THE ASTROPHYSICAL JOURNAL, 375:264–287, 1991 July 1

ANALYSIS OF SN 1987A POLARIMETRY

DAVID J. JEFFERY[1]
Department of Physics and Astronomy, University of Oklahoma, Norman, OK 73019
Received 1990 July 9; accepted 1991 January 2

ABSTRACT

Models and a polarized radiative transfer technique useful for analyzing the SN 1987A polarimetric data are introduced and discussed. Demonstration results calculated using the models are presented. An interstellar polarization correction needed for analyzing the SN 1987A polarimetric data is introduced. A summary and interpretation of the evolution of the SN 1987A polarization that relies on this correction is given. An analysis of a small selection of the SN 1987A polarimetry is reported. The important conclusions of this analysis are that the SN 1987A continuum polarization and line polarization features are mostly due to the polarizing effect of electron scattering and that there is probably an excitation asymmetry in SN 1987A. An interpretation of the SN 1987A polarimetric data in terms of simple shape asymmetry requires that SN 1987A have a length-width difference of order 10% or more.

Subject headings: polarization — stars: individual (SN 1987A) — stars: supernovae

1. INTRODUCTION

Polarimetric observations of SN 1987A revealed a significant polarization of the supernova's flux. Since the polarization is time-dependent and its wavelength dependence is correlated with the flux line features, it is clear that the polarization is to a large degree intrinsic, although a significant interstellar polarization is also certainly present in the observations. Because the continuous opacity of SN 1987A's atmosphere is thought to be dominated by electron scattering opacity (Höflich 1988; Eastman & Kirshner 1989), the flux emitted from the supernova is expected to be polarized. Of course, however polarized the supernova's emergent specific intensity beams are, there would be no net polarization if the supernova is spherically symmetric. Analyses of the SN 1987A polarimetric observations using simple axisymmetric oblate or prolate supernova ejecta models (Cropper et al. 1988; Méndez et al. 1988; Höflich, Sharp, & Zorec 1989) suggest that SN 1987A possessed some sort of length-width asymmetry in the range $\sim 5\%$ to $\sim 30\%$. In this paper, an analysis of a small selection of the SN 1987A polarimetry is reported that uses a more advanced polarized radiative transfer technique than that used in previous papers. The aims of this analysis are to understand how SN 1987A continuum and line polarization arise and to investigate the nature of the SN 1987A asymmetry. The supernova models used in the analysis again assume only simple axisymmetric prolate and oblate asymmetries. The assumption of axisymmetric asymmetry is known at the outset to be too simple, but it is a simplifying and probably partially valid assumption (see § 6.2). Aside from the actual analysis given, the purpose of this paper is to present and discuss the models and the procedures that will be useful in future, more complete analyses of the SN 1987A polarimetry.

In considering the SN 1987A observations, it is useful to specify the epoch consistently. Therefore, throughout this paper the SN 1987A epoch will be specified relative to the neutrino event of 1987 February 23.316 UT (Bionta et al. 1987; Hirata et al. 1987), e.g., day 2 for 1987 February 24 UT. Since the duration of the neutrino event and the time difference between the core collapse and the neutrino event are insignificant compared with the time scale of spectral evolution after day 1, the time of the neutrino event will be referred to simply as the time of explosion.

Section 2 of this paper introduces the Sobolev-P method, which is the polarized radiative transfer technique used for the calculations. The spherically symmetric supernova model and the two aspherical supernova models used in the analysis are introduced in § 3. Section 4 presents some demonstration results of the synthetic spectrum calculation procedure and compares results calculated using the two aspherical supernova models. Section 5 discusses the interstellar polarization estimate that is used to correct the SN 1987A polarimetry and other corrections for the SN 1987A data. In § 6, a summary and interpretation are given of the evolution of the SN 1987A polarization, a selection of the SN 1987A polarimetry is presented and analyzed using fitted synthetic polarization spectra, and a discussion of the possible origin of the SN 1987A asymmetry is given. Conclusions and discussion are given in § 7. The Appendix presents and discusses some simple analytical expressions that aid in understanding the polarized radiative transfer.

2. POLARIZED RADIATIVE TRANSFER WITH THE SOBOLEV-P METHOD

The technique used for calculating the radiative transfer is the Sobolev-P method that has been developed in earlier works (Jeffery 1988, 1989, 1990, hereafter SPM I, SPM II, and SPM III, respectively). The Sobolev-P method is a generalization of the Sobolev method (Sobolev 1947) that takes account of the polarization state of radiation and allows for the polarizing effect of line scattering. In this paper it is assumed that the reader is familiar with the Sobolev method, line formation in expanding atmospheres, and radiative transfer in general and thus understands the usage of terms such as line saturation, line blanketing, source function, P Cygni line profile, Sobolev optical depth, escape probability, resonance region, and CD (common direction) and CP (common point) velocity surfaces. Useful references for the Sobolev method are the important papers of Rybicki & Hummer (1978) and Olson (1982). A derivation of the Sobolev method is also presented by Jeffery & Branch (1990, hereafter JB) along with a catalog of

[1] Present address: Harvard-Smithsonian Center for Astrophysics, 60 Garden Street, Cambridge, MA 02138.

illustrative Sobolev method calculation results for model supernova atmospheres.

Like the Sobolev method, the Sobolev-P method is an approximate technique that is only appropriate for calculating line radiative transfer in systems with large velocity gradients. For supernovae, which all have very large velocity gradients, Sobolev-type calculated line spectra are expected to agree with more accurate line spectra calculated with the comoving-frame formalism, usually to within much less than 10% of the continuum flux level in the vertical direction and to order $\lambda_0(v_{ra}/c)$ in the horizontal direction, where λ_0 is a line-center wavelength and v_{ra} is the characteristic velocity of the small-scale random motions (i.e., thermal motions and perhaps small-scale fluid-element motions) in the atmosphere. The accuracy of the Sobolev method has been investigated by Hamann (1981) and is discussed for the case of supernovae by JB.

In the Sobolev-P method, the scalar specific intensity and source function of the Sobolev method are replaced by analogous Stokes vector quantities. The Stokes vectors have four components, which are the Stokes parameters. The Sobolev-P method uses Chandrasekhar's version of the Stokes parameters: I_l, I_r, U, and V (Chandrasekhar 1960, p. 34). The I_l and I_r parameters are the specific intensity components along axes labeled l and r; these axes are perpendicular to each other and to the direction of radiation propagation. The conventional Stokes I parameter (the ordinary specific intensity) and Q parameter are related to I_l and I_r by

$$I = I_l + I_r \quad \text{and} \quad Q = I_l - I_r \,. \tag{1}$$

Polarization is given by

$$P = \frac{(Q^2 + U^2)^{1/2}}{I} \times 100\% \tag{2a}$$

or

$$P = \frac{Q \cos 2\chi + U \sin 2\chi}{I} \times 100\% \,, \tag{2b}$$

where χ is the position angle (p.a.) of polarization measured clockwise from the l-axis and the introduction of a factor of 100% is a convention adopted in this paper (as in many other places) so that polarization is measured in percent. The position angle is given by

$$\chi = \tfrac{1}{2} \arctan (U/Q) + k\pi/2 \,, \tag{3}$$

where the factor k is an integer chosen in order to make equations (2a) and (2b) consistent. Note that position angles differing by multiples of π (180°) are physically identical. Because of symmetry, the position angle of polarization of flux emitted by an axisymmetric system can have only two values: 0° or 90° with respect to the symmetry axis. Thus, the position angles obtained from axisymmetric calculations will always be confined to two values which are 90° apart.

The Sobolev method assumes complete wavelength and angular redistribution for line scattering. Complete wavelength redistribution means that the wavelengths of the incident and scattered photons are uncorrelated. Complete angular redistribution means that the scattered photons are emitted isotropically and are unpolarized. The Sobolev-P method retains the assumption of complete wavelength redistribution, but treats angular redistribution with a phase matrix that gives rise to anisotropic and polarizing scattering. The inclusion of this phase matrix complicates the expressions for the Stokes source vector, which is the Stokes vector analog of the source function. The expressions for the Sobolev-P method Stokes source vector are given in SPM II for axisymmetric systems and in SPM III for three-dimensional systems.

The phase matrix used to treat scattering in the Sobolev-P method was derived by Hamilton (1947). This Hamilton phase matrix is a linear combination of the Rayleigh matrix (modified by an extra factor multiplying the matrix element determining circular polarization) and the isotropic scattering phase matrix. Since the sum of the coefficients of the two matrices in the linear combination is normalized to 1, only the coefficient of the Rayleigh phase matrix is needed to determine the polarizing effect of a line. This coefficient, called the E_1 coefficient, is 0 for a nonpolarizing line and 1 for a line that polarizes like an electron. The expressions for the E_1 coefficient depend only on the lower- and upper-level total angular momenta of a given line. For $\frac{1}{2}$–$1\frac{1}{2}$ and 0–1 lines the E_1 coefficients are $\frac{1}{2}$ and 1, respectively. For all other lines, the E_1 coefficients are between 0 and 0.4. Clearly, most scattering by lines will be considerably less polarizing and sometimes much less polarizing than electron scattering. The expressions for the E_1 coefficients are given in Table 1 of SPM II. Tables 3 and 6 in SPM II give the E_1 coefficients for lines with $j_l \leq 6\frac{1}{2}$ and the mean E_1 coefficients for LS coupling multiplets, respectively.

There is no evidence for significant circular polarization of the SN 1987A flux through day 198 (Barrett 1988). Since the V Stokes parameter, which measures circular polarization, is not coupled by the Rayleigh or isotropic scattering phase matrices to the other Stokes parameters (Chandrasekhar 1960, pp. 42 and 51; SPM II), the absence of circular polarization in the emergent SN 1987A flux shows that circular polarizing effects are probably negligible in the radiative transfer through the SN 1987A atmosphere. Consequently, circular polarization is not considered further in this paper.

The Sobolev-P method's treatment of the intrinsic polarizing effect of line scattering is probably only qualitatively accurate, since the assumed photon redistribution behavior is only a crude approximation. In real line scattering there is coupling between angular and wavelength redistribution in the comoving frame and correlation between the incoming and outgoing photon wavelengths. The Sobolev-P method assumes that the Hamilton phase matrix applies to all lines, but this matrix was in fact derived only for resonance lines (i.e., lines where the line lower levels are ground levels). No allowance is made for the depolarizing effect that weak collisions have on photon redistribution. (Weak collisions can cause excited levels to lose directional information about the exciting line photons, and consequently the line-emitted radiation is isotropic and unpolarized.) The degree of error introduced by these deficiencies should be investigated by comparisons of Sobolev-P method line polarization results with the line polarization results of more exact techniques. Such comparisons remain to be done. Arguments for the qualitative accuracy of the Sobolev-P method are given in SPM I (p. 74) and SPM II. For the present, only the depolarizing effect of weak collisions needs further discussion, since this effect can eliminate the intrinsic polarizing effect of lines altogether.

Order-of-magnitude estimates have shown that the depolarization effect of weak collisions probably will not destroy the intrinsic line polarizing effect in the outer line-forming layer of a supernova atmosphere. In the deeper line-forming layer, it seems likely that the intrinsic line polarizing effect will be destroyed. However, the intrinsic line polarizing effect tends to

be physically redundant in the deeper layers. In these regions, the multiple scatterings that photons undergo in multiple resonance regions and with continuous opacity scatterers will tend to keep the radiation field rather isotropic and unpolarized even with polarizing scattering by lines and continuous opacity scatterers. It is the last few scatterings that a photon escaping the atmosphere undergoes that are most significant for net polarization of the emergent spectrum. (The effect of multiple scatterings on the polarizing power of a resonance region is discussed in the Appendix.) Therefore, including the intrinsic line polarizing effect deep in the atmosphere is probably at worst a small error. The important question is how significant is the uncertainty about the intrinsic line polarizing effect in the outer layers. The results of many test calculations have shown that this uncertainty is not very significant because the intrinsic line polarizing effect is of secondary importance in the formation of the line polarization features. The line polarization features are chiefly formed by the interaction of the electron polarized flux and the lines acting as depolarizing scatterers and as global flux redistributors. The lines act as depolarizing scatterers even when they are intrinsically polarizing, because almost all lines have E_1 coefficients that are considerably less than 1 (see above). The electron and line polarizing effects are discussed further in § 4.

The only continuous opacity included in the radiative transfer is electron scattering opacity (see § 3.1). Thus, free-free opacity, bound-free opacity, and expansion opacity are being ignored. (The expansion opacity is a quasi-continuous opacity due to thousands of weak lines. The opacity of these weak lines is enhanced by the macroscopic velocity field; Karp et al. 1977.) The expansion opacity is probably the most important of the neglected opacities (Wagoner 1981), since it can be of the same order of magnitude as the electron opacity. Since the polarizing effect of lines is considerably smaller than the polarizing effect of electron scattering, the assumption that all continuous opacity is electron opacity will tend to cause the global polarizing effect of model atmospheres to be enhanced. Thus, the use of only electron opacity for the continuous opacity will tend to minimize the model asymmetry needed to fit observations.

The electron scattering opacity is treated using the discretized continuous opacity (DCO) approximation developed in SPM II. The DCO approximation replaces the continuous opacity with closely spaced pseudolines. The electron pseudolines are made to behave as pure resonance scattering lines (i.e., as two-level atom lines where only radiative transitions are allowed) with E_1 coefficients equal to 1; this behavior is exactly correct for electron scattering. For an atmosphere with large velocity gradients, the replacement of continuous opacity by pseudolines is equivalent to a spatial discretization of the continuous opacity. Wavelength discretization is, however, simpler to implement than spatial discretization, since it allows line and continuous opacity to be treated in the same manner. The prescription for the pseudoline Sobolev optical depth, derived in SPM II, is

$$\tau(r) = \frac{\Delta\lambda}{\lambda_{ps}} \frac{c}{|dv/ds|} \frac{\tau_{ph}(\text{con})}{F_{ph}} f(r) , \tag{4}$$

where λ_{ps} is the line-center wavelength assigned to the pseudoline, $\Delta\lambda$ is the wavelength discretization increment, dv/ds is the derivative of the velocity along a beam path with coordinate s, $\tau_{ph}(\text{con})$ is the continuum optical depth to the photosphere (see § 3.1 for the definition of the photosphere used in this paper), $f(r)$ is a dimensionless distribution function for the continuous opacity which is chosen so that $f(r)$ is 1 at the photosphere, and

$$F_{ph} = \int_{r_{ph}}^{R} dr' f(r') , \tag{5}$$

where r_{ph} is the photospheric radius and R is the outer cutoff radius of the atmosphere. In uniform-motion homologous expansion (see § 3.1) dv/ds is a constant for all locations and directions.

For the calculations reported in this paper, the prescription used for determining the pseudoline wavelength increment is

$$\frac{\Delta\lambda}{\lambda_{ps}} = X_{ph} \frac{v_{ph}}{c} , \tag{6}$$

where v_{ph} is the photospheric velocity (see § 3.1) and X_{ph} is a free parameter. When $X_{ph} \approx 1$, the P Cygni trough flux and polarization features of one pseudoline will overlap the emission flux and polarization features of the next bluer pseudoline (see § 3.1 for a discussion of P Cygni line profile widths). The condition $X_{ph} \lesssim 1$ is usually needed for the pseudolines to produce even an appearance of a continuous opacity. No good criterion has been established for the size of X_{ph} necessary for establishing true continuous opacity behavior. When calculating synthetic spectra with a given set of model parameters, one reduces X_{ph} until the spectra converge. Convergence for the flux spectrum occurs when the flux spectrum stops changing except for an overall scale factor. The fact that a scale factor uncertainty remains shows that the radiative transfer deep in the model has not converged to true continuum radiative transfer. If one keeps reducing X_{ph} (i.e., using more pseudolines) after convergence, the scale of the flux spectrum decreases. Clearly, the narrower the pseudoline wavelength increment, and consequently smaller the pseudoline optical depths, the more efficient the pseudolines are at scattering photons back to the core (see § 3.1 for the definition of the core) where in the physical picture they are absorbed. Convergence for the polarization spectrum occurs when the polarization spectrum stops changing in shape and scale as X_{ph} is reduced. In judging convergence, small oscillations superposed on the spectra due to the finite wavelength increment of the pseudolines can usually be ignored. With a smaller wavelength increment and, of course, more computational labor, these oscillations can be reduced.

Because of calculational limits, the pseudolines cannot be extended over all wavelengths. In order to establish a specified wavelength range of continuous opacity behavior, the pseudolines must be extended over a somewhat large wavelength range. At the edges of the pseudoline range spurious line features will appear. The size of the pseudoline range should be increased until the flux and polarization behavior in the specified range of continuous opacity behavior stops changing, i.e., converges. For all the calculations with DCO reported in this paper, the pseudoline ranges were chosen sufficiently large that no spurious line features from the edges of the pseudoline ranges appear in the figures.

Although no good criterion for convergence has been worked out, an argument can be made that the pseudoline optical depths especially above the photosphere (see § 3.1) should be less than about 1. In order to keep the computational labor as small as possible, the wavelength increment used in the DCO approximation will usually be chosen large compared with the line widths of real lines. The wavelength

increment can be regarded as the line width of the pseudolines. Thus, the pseudolines will tend to be broad compared with real lines. Sobolev-type methods treat all lines as if their line widths, and consequently their spatial resonance region widths, were zero. This approximation is valid as long as physical quantities are rather constant across the resonance regions. This constancy criterion is harder to meet for lines with larger line widths and consequently larger resonance region widths. The deviations from exact results that occur in Sobolev method calculations because of finite line widths have been investigated by Hamann (1981). These deviations become smaller as line optical depth becomes smaller and, in particular, are expected to be qualitatively reduced when the line optical depth is reduced below about 1 (see, e.g., JB). Therefore, having the pseudoline optical depths less than about 1 is expected to be a useful criterion at least for beginning a search for convergence. Since one especially wants to get the continuum radiative transfer near the surface correct in order to get the emergent flux and polarization spectra correct, satisfying the criterion at and above the photosphere is particularly desirable.

Quantitatively accurate calculations of continuum flux and polarization behavior with the DCO approximation can be made. This is demonstrated in § 4 and in SPM II by the comparison of DCO approximation results to exact results. It should be remarked that it has not been demonstrated that the DCO approximation can be made numerically accurate for atmospheres with continuum optical depths greater than 10.

3. SUPERNOVA MODELS

Three supernova models are used for the calculations reported in this paper: a spherically symmetric model, a heuristic axisymmetric model with an elliptical projection (hereafter "the heuristic model"), and a true two-dimensional axisymmetric ellipsoidal model (hereafter "the realistic model"). Since the two aspherical models are straightforward generalizations of the spherically symmetric model, the common features of the three models are treated in § 3.1, which nominally describes the spherically symmetric model. The aspherical models are, of course, the essential models for this paper, since they are the models that can produce a polarized net flux. The use of axisymmetric aspherical models is plausible, since axisymmetry has a natural explanation in the rotation of the supernova progenitor. Whether rotation will result in prolate, oblate, or some combination of prolate and oblate asymmetry is still not certain (see the discussion of asymmetry in § 6.3). The heuristic and realistic models are described in §§ 3.2 and 3.3, respectively.

3.1. *The Spherically Symmetric Model*

The spherically symmetric model consists of a spherically symmetric distribution of supernova explosion ejecta in uniform-motion homologous expansion. (Uniform-motion homologous expansion is discussed by, e.g., JB. All the observations considered in this paper come from the homologous epoch of SN 1987A.) The ejecta is divided into two regions: a continuum radiation field emitting core and a scattering atmosphere. The model is highly parameterized.

The comoving-frame density of the ejecta in the homologous epoch decreases everywhere in proportion to t^{-3}. Therefore, the homologous epoch density distribution can be conveniently specified by specifying ρt^3 everywhere in the comoving frame; hereafter, the ρt^3 distribution will be called the homologous density distribution. For the (spherically symmetric, heuristic, and realistic model) demonstration calculations reported in § 4, the homologous density distributions used are simply inverse power laws of the radius. The homologous density distribution adopted for the (heuristic model) spectrum-fit calculations reported in § 6.2 in a slightly modified version of the empirical SN 1987A homologous density distribution given by JB (see JB, Fig. 18*a*). The JB homologous density distribution was derived using many simplifying assumptions, including spherical symmetry, from the SN 1987A photometric data given by Catchpole et al. (1987, 1988). The modification of the JB homologous density distribution made for this paper is merely a smoothing of an inflection that occurred near 7500 km s^{-1}; JB determined that this inflection gave rise to features in synthetic spectra that were not present in observed spectra. Figure 1 shows the (modified) JB homologous density distribution with radial velocity serving as the comoving-frame coordinate.

The JB homologous density distribution can be broken into segments that roughly obey inverse power laws of velocity. The inverse power law indices for the regions with velocity less than 1400 km s^{-1}, 1500–2200 km s^{-1}, 2200–5000 km s^{-1}, 5000–9000 km s^{-1}, 9000–10,000 km s^{-1}, and greater than 10,000 km s^{-1} are roughly 1.8, 2.5, 5, 4, 12, and 13, respectively. For velocities higher than 10,000 km s^{-1}, the distribution is logarithmically extrapolated from the outermost two points of the distribution displayed in Figure 1. The actual density values for any epoch (which can be obtained from Fig. 1) are very uncertain because of the many assumptions used in deriving the JB homologous density distribution. Actual density values are not used in the calculations. Only the relative homologous density distribution is needed for use as a scaling function (see below).

The continuum radiation field emitted by the core is a blackbody radiation field for the (heuristic model) spectrum-fit calculations reported in § 6.2. Since the core matter is participating in the homologous expansion, the specific intensity beam emitted from the core has an angle-dependent Doppler shift in any comoving frame other than the comoving frame of emission itself and in the observer frame. The temperature used for the blackbody radiation field for a given SN 1987A epoch is obtained by interpolating from the tabulated SN 1987A color temperatures given by Catchpole et al. (1987, 1988). The continuum fluxes obtained using color temperatures were found by JB to be adequate for synthetic spectrum fitting; discrepancies particularly in the *B* band between the synthetic and observed continuum fluxes in JB's figures can plausibly be attributed to line blanketing. For the (spherically symmetric, heuristic, and realistic model) demonstration calculations reported in § 4, a wavelength-independent radiation field is emitted by the core. The use of a wavelength-independent radiation field eliminates one complicating effect in understanding the formation of synthetic flux and polarization spectra.

The widths of P Cygni line profile features, and in particular the blueshift of the P Cygni trough minimum from the line-center wavelength, depend on the distributions of continuous opacity and Sobolev optical depth with velocity. The important atmosphere region for P Cygni line profile formation is located at a radial total continuum optical depth of order unity. (Total continuum optical depth is the sum of absorption and scattering optical depths.) This region is usually called the photosphere. For convenience in this paper, the photosphere is defined to be the atmosphere region at exactly radial total continuum optical depth 1. For strong lines (i.e., those with a

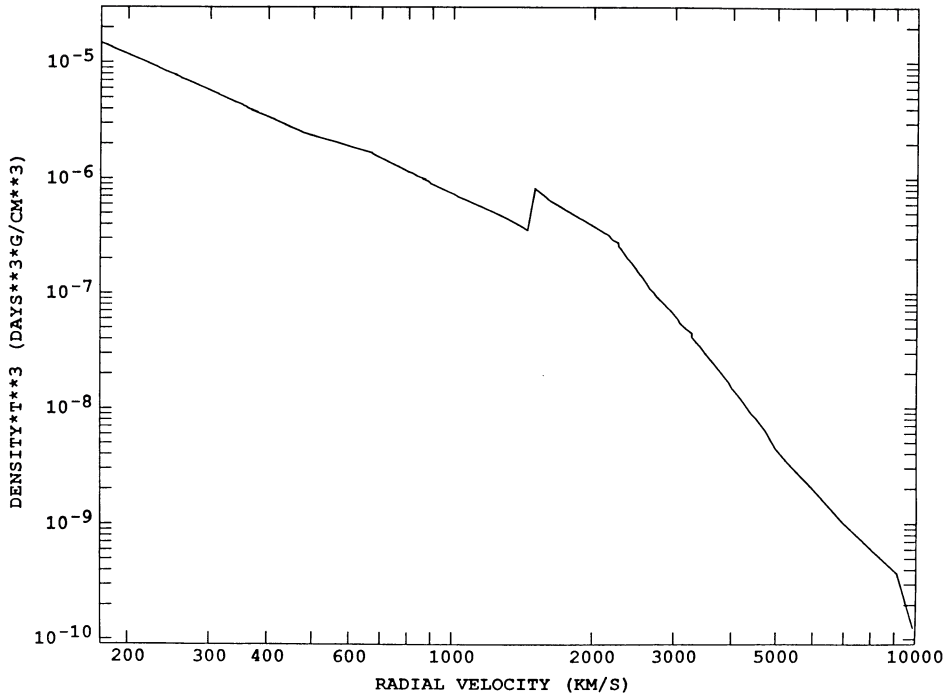

FIG. 1.—JB homologous density distribution

photospheric Sobolev optical depth $\tau_{ph} \gg 1$), the trough minimum flux forms in CD velocity surfaces where the effective average Sobolev optical depth is of order 1 and that are in front of the photosphere (i.e., are nearer the observer than the photosphere). The line-of-sight velocity of these surfaces relative to the center of the expansion gives rise to the blueshift of the trough minimum. For weak lines (i.e., those with $\tau_{ph} \lesssim 1$), the trough minimum flux tends to form in the CD velocity surfaces that are approximately tangent to that part of the photosphere nearest the observer. Thus, the blueshifts of the trough minima of weak lines tend to correspond to the line-of-sight matter velocity at that part of the photosphere nearest the observer (see, e.g., Eastman & Kirshner 1989). This velocity, called the photospheric velocity, is clearly an important parameter for spectrum formation. Because of the many complicated effects in a real atmosphere, there probably will not be a unique photospheric velocity for all wavelength regions and all weak lines. However, using a unique photospheric velocity for a synthetic spectrum seems to be an adequate approximation. The SN 1987A photospheric velocities used in the (heuristic model) spectrum-fit calculations reported in § 6.2 were taken from JB (see JB, Fig. 16).

The Sobolev optical depths of the lines are parameterized in the following way. The photospheric Sobolev optical depth τ_{ph} of a chosen strong line of an ion is taken as a fitting parameter. The photospheric optical depths for all the other lines for this ion are then determined by assuming that level occupation numbers obey the Boltzmann law at a specified excitation temperature. For the (heuristic model) spectrum-fit calculations reported in § 6.2, the SN 1987A color temperature is used as the excitation temperature; the (spherically symmetric, heuristic, and realistic model) demonstration calculations reported in § 4 did not require an excitation temperature, since only one real line was included in each calculation. The optical depths above and below the photosphere are obtained by scaling photospheric optical depths with the assumed homologous density distribution of the supernova ejecta.

The line Stokes source vectors are assumed to be due to pure resonance scattering. With this assumption, only radiative transitions are allowed between the upper and lower levels of each line, and the line levels are treated as if they were uncoupled from all other atomic levels.

The simple scaling parameterization for the Sobolev optical depths and the use of pure resonance scattering are both sweeping and highly simplifying assumptions. The Sobolev optical depths and line source functions ought to be calculated from occupation numbers determined by detailed non–LTE (NLTE) calculations. Such NLTE calculations are beyond the scope of the research reported here and are for the present probably computationally too demanding to be undertaken for asymmetric (i.e., non–spherically symmetric and non–plane-parallel) atmospheres. Occupation numbers and hence the Sobolev optical depths calculated in NLTE may deviate from the simple scaling parameterization values by an order of magnitude or more. There is unfortunately no simple way to predict the size or direction of these deviations; LTE occupation numbers, for instance, can also show deviations from NLTE calculated occupation numbers of an order of magnitude or more (e.g., Branch et al. 1991). Since line source functions (and line Stokes source vectors) depend on ratios of occupation numbers, it is plausible that the pure resonance scattering line source functions will have smaller errors than the simple scaling parameterization Sobolev optical depths. In fact, limited NLTE calculations for supernova atmospheres (Feldt 1980) suggest that the line source functions calculated assuming pure resonance scattering are often correct to within a factor of 2. Unfortunately, the pure resonance scattering approximation is not a very good approximation for the Hα

line in Type II supernova (SN II) atmospheres; the Hα line profiles in SN II spectra usually show net emission which cannot be produced by pure resonance scattering.

Having roughly the correct radiation flow geometry is necessary for calculating polarization. On the local scale, this is because polarization due to scattering depends on the scattering angle and thus on the angular variation of the radiation field convergent on a point scatterer. On the global scale, the rediation flow geometry helps to determine the net polarization. Synthetic supernova flux spectra calculated with the scaling parameterization and pure resonance scattering can usually be fitted closely to observed flux spectra from the photospheric phase (see definition below) by adjusting model parameters (see, e.g., Branch et al. 1985; JB). The quality of the fits obtained is evidence that the radiation flow geometry can be roughly correctly calculated even when the complex line interlocking effects are being ignored.

The pure resonance scattering assumption artificially heightens the polarizing power of line interactions, since the coupling of lines is almost certainly a depolarizing effect. However, any polarization error introduced in this way turns out to be unimportant, since, as discussed in §§ 2 and 4, the intrinsic line polarizing effect is of secondary importance in the formation of the line polarization features.

The two continuum optical depth parameters of the model are the radial photospheric continuum optical depth $\tau_{ph}(\mathrm{con})$ and the radial core continuum optical depth $\tau_{core}(\mathrm{con})$. The continuous opacity that gives rise to these optical depths is assumed to be pure electron scattering opacity; the neglected forms of continuous opacity were discussed briefly in § 2. The definition of photosphere that is adopted requires that $\tau_{ph}(\mathrm{con})$ be set to 1 always. The core of the model is intended to represent crudely the thermalization layer, where radiation and matter are in thermodynamic equilibrium. A well-known crude analytic result is $\tau_{th}(\mathrm{con}) \sim (3\xi)^{-1/2}$, where $\tau_{th}(\mathrm{con})$ is the radial total continuum optical depth to the thermalization layer and ξ is some kind of atmosphere average of the ratio of absorption opacity to total opacity (e.g., Mihalas 1978, p. 149). From Höflich's NLTE calculations (1988) it appears that ξ in the SN 1987A atmosphere ranges between of order 10^{-2} and of order 10^{-1} during at least the first 200 days after the explosion. Thus, for SN 1987A, $\tau_{th}(\mathrm{con})$ is very crudely estimated to range between 2 and 6 for that period. In order to approximate the SN 1987A continuum thermalization optical depths, the value of $\tau_{core}(\mathrm{con})$ was set to 3 for all (heuristic and realistic model) demonstration calculations reported in § 4. Numerical experiments with the models used for this paper have shown that the emergent flux and polarization spectra do not vary much with $\tau_{core}(\mathrm{con})$ for $\tau_{core}(\mathrm{con}) \gtrsim 3$. One should note that the behavior of continuum polarization as a function of $\tau_{core}(\mathrm{con})$ is model-dependent. For example, Daniel (1978) shows some of the various behaviors that can occur for prolate and oblate models with point cores.

The numerical value of the photospheric radius r_{ph} can be chosen arbitrarily, since its value is merely a question of units. For convenience, the photospheric radius has been set to 1 always. Having set the values of r_{ph}, $\tau_{ph}(\mathrm{con})$, and $\tau_{core}(\mathrm{con})$, the core radius, r_{core}, can be solved for from

$$\tau_{core}(\mathrm{con}) = \frac{\tau_{ph}(\mathrm{con})}{F_{ph}} \int_{r_{core}}^{R} dr' f(r') \; ; \qquad (7)$$

recall that R is the outer cutoff radius of the atmosphere. The distribution function $f(r)$, which is proportional to the electron density distribution, can be chosen to scale with the homologous density distribution just like the Sobolev line optical depths. For SN 1987A up to about day 5, choosing electron density to scale with density is a good approximation, since the hydrogen is well above the recombination temperature ($\sim$5500 K). At later times this scaling approximation is very crude, and NLTE calculations are needed to establish accurate electron densities. In order to make up for any obvious deficiencies of the scaling approximation in the fitting procedure, the $f(r)$ function can be chosen to have different behavior: e.g., an inverse power law behavior with the index as a free parameter. When the JB homologous density distribution is used for $f(r)$, the solution of equation (7) for r_{core} must be obtained numerically. The optical depths of the pseudolines are determined using $f(r)$ and the prescriptions given in § 2.

The first phase of supernova spectral evolution is called the photospheric phase. This phase is characterized by P Cygni line profiles. The end of the photospheric phase can be roughly defined as the time when the spectrum begins to be dominated by emission-line profiles, including those for forbidden transitions. For all types of supernovae, the spectra seem to become dominated by emission-line profiles very roughly speaking 6 months after maximum light. Since some P Cygni line trough features may persist for hundreds of days after strong emission-line profiles appear, a clear-cut ending of the photospheric phase is not easily definable. The period after the end of the photospheric phase can be called the early nebular phase. When the continuum optical depth to the ejecta center falls below 1, a supernova can be said to be in the (full) nebular phase. Unfortunately, it is not yet determinable exactly when the continuum optical depth to the ejecta center falls below 1 from observations or from detailed modeling. Clearly, the spherically symmetric model with its continuum radiation field emitting core and assumption of pure resonance scattering can only be an appropriate model for the photospheric phase. (The spectral evolution of supernovae is reviewed by, e.g., Wheeler 1990.)

3.2. *The Heuristic Model*

The heuristic model is essentially the spherically symmetric model with a minor modification in the calculation of the polarization of the net flux. This modification is a plausible means to extract from the spherically symmetric model some of the behavior of a real aspherical axisymmetric ellipsoidal model. The idea for the modification is taken from McCall (1984, 1985).

Consider the projection of a spherically symmetric atmosphere. Let the radius of the photodisk (i.e., the projection of the photosphere) be set to 1 for convenience. Let there be a y-z coordinate system with an origin at the center of the projection. From every point on the projection, a beam is emitted toward the observer. For each point, the local l- and r-axes are defined to be parallel and perpendicular, respectively, to the radius to that point. Spherical symmetry requires that the U Stokes parameter of a beam emitted from a point be zero in the local l-r system. Thus, the polarization of a beam is aligned parallel or perpendicular to the radius to the emitting point. Let the circle defined by each radius be distorted into an ellipse that has c/a as its ratio of z semiaxis to y semiaxis, and let the z and y semiaxes of the distorted photodisk be c and a, respectively. Each point's new elliptical projection coordinates (y, z)

are related to its old circular projection coordinates (y', z') by

$$y = ay' \quad \text{and} \quad z = cz' . \tag{8}$$

Let the radius of a former circle be denoted by g. The g-values are related to the new coordinates by

$$g = [(y/a)^2 + (z/c)^2]^{1/2} . \tag{9}$$

Let the specific intensity and its polarization be the same for each point before and after the distortion. Thus, these quantities depend only on g, and that dependence is unchanged by the distortion. For the new elliptical projection, the polarization of a beam is taken to be aligned parallel or perpendicular to the tangent to the curve defined by equation (9) that passes through the point of beam emission. Thus, by defining the local l and r-axes for the elliptical projection to be perpendicular and parallel, respectively, to this tangent, the U Stokes parameter in the local l-r system is automatically zero. It is this spherically symmetric system with an elliptically distorted projection that constitutes the heuristic model. A schematic diagram of the heuristic model is shown in Figure 2.

In order to calculate the polarization of the heuristic model net flux, the Stokes parameters for each local l-r system must be transformed to a common l-r system. Using the y-z system for the common l-r system (z for l and y for r) and the transformation equations for the Stokes parameters (see, e.g., Chandrasekhar 1960, p. 34), one finds

$$I_z = I_l \cos^2 \gamma + I_r \sin^2 \gamma \tag{10a}$$

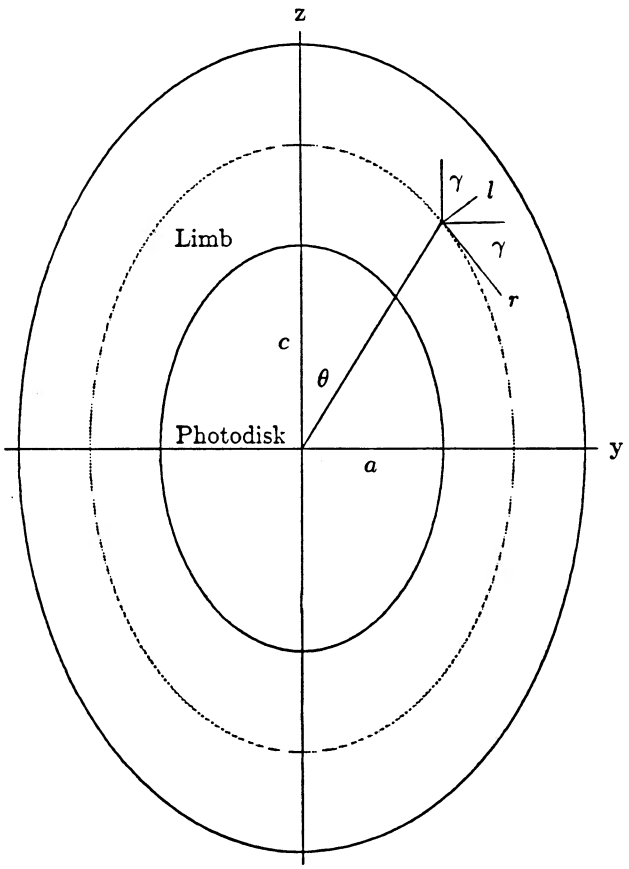

FIG. 2.—Schematic diagram of the heuristic model

and

$$I_y = I_l \sin^2 \gamma + I_r \cos^2 \gamma , \tag{10b}$$

where the terms involving the local l-r system U Stokes parameter vanish, since this parameter is zero, and where γ is the angle between the local l-axis and the z-axis (see Fig. 2). Note that the global U and V Stokes parameters are automatically zero because of symmetry. Expressed as functions of θ, the angle between the z-axis and the radius to whatever point is being considered,

$$\cos \gamma = \frac{1}{[1 + (c/a)^4 \tan^2 \theta]^{1/2}} \tag{11a}$$

and

$$\sin \gamma = \frac{(c/a)^2 \tan \theta}{[1 + (c/a)^4 \tan^2 \theta]^{1/2}} . \tag{11b}$$

The integration for the net Stokes parameters must be done over the y-z plane. If one uses the transformation given by

$$y = ag \sin \xi , \quad z = cg \cos \xi , \quad dy\, dz = acg\, dg\, d\xi , \tag{12}$$

the integrations over the two coordinates can be separated. One obtains

$$F_l = ac \int_0^{g_{\max}} dg\, g I_l , \tag{13a}$$

$$F_r = ac \int_0^{g_{\max}} dg\, g I_r , \tag{13b}$$

$$4 \int_0^{\pi/2} d\xi \cos^2 \gamma = 4 \int_0^{\pi/2} d\xi \frac{1}{1 + (c/a)^2 \tan^2 \xi} = 2\pi \left[\frac{1}{1 + (c/a)} \right] , \tag{13c}$$

and

$$4 \int_0^{\pi/2} d\xi \sin^2 \gamma = 4 \int_0^{\pi/2} d\xi \frac{(c/a)^2 \tan^2 \xi}{1 + (c/a)^2 \tan^2 \xi} = 2\pi \left[\frac{(c/a)}{1 + (c/a)} \right] , \tag{13d}$$

where symmetry allows the integration over 2π to be replaced by integration over $\pi/2$ and an extra factor of 4. The polarization of the net flux is then given by

$$P = \left| \left(\frac{F_l - F_r}{F_l + F_r} \right) \left[\frac{1 - (c/a)}{1 + (c/a)} \right] \right| \times 100\% . \tag{14}$$

Recalling equation (2) and the fact that the Stokes U parameter of the net flux is zero, the position angle of polarization is given by

$$\chi = \begin{cases} 0 & \text{for } (F_l - F_r)[1 - (c/a)] > 0 , \\ \pi/2 & \text{for } (F_l - F_r)[1 - (c/a)] < 0 , \end{cases} \tag{15}$$

where χ is measured clockwise from the z-axis. Any spherically symmetric atmosphere with Rayleigh-type scattering that is easily imaginable will have $F_l < F_r$. This is easily understood. In Rayleigh-type scattering, the scattered specific intensity component perpendicular to the plane of scattering (i.e., the plane containing the scattered and incident beams) is always larger than or equal to the scattered specific intensity com-

ponent parallel to the plane of scattering. For most astrophysical atmospheres, the anisotropic radiation field at the surface is outward-peaked (i.e., the specific intensity beams are stronger perpendicular to the surface than parallel to the surface). Thus, with both Rayleigh-type scattering and outward peaking at the surface, one usually expects that the emergent r-beam will be stronger than the emergent l-beam, and therefore that the polarization will align parallel to the atmosphere surface. This polarization alignment effect is shown by the plane-parallel atmosphere investigated by Chandrasekhar (1960, p. 248) and the spherically symmetric atmospheres investigated by Cassinelli & Hummer (1971). Given the above arguments, it follows that the position angle of the polarization of the heuristic model will align with the long axis of the heuristic model in all easily foreseeable cases.

From equation (14), it is clear that the polarization at all wavelengths will scale by a common factor as the parameter c/a is varied. The total flux of the heuristic model at all wavelengths will scale with the factor ac. In this paper, the absolute scale of the flux is undetermined and of no interest. Therefore, the flux of the heuristic model is for all present purposes the same as the flux of the spherically symmetric model.

The question now arises, how adequate is the heuristic model as an approximation to a true axisymmetric ellipsoidal model such as the one introduced in § 3.3? Clearly, the average properties of the radiation field and the source functions of the heuristic model should be qualitatively adequate, since these are just those of the spherically symmetric model which is a true extended atmosphere model (see § 4 for a discussion of extended atmospheres). But, one asks, can the difference of the global l and r fluxes have anything like the right behavior? A simple physical picture can be introduced in order to investigate this question.

Consider a spherically symmetric atmosphere that is elongated into a prolate atmosphere or flattened into an oblate atmosphere. If one assumes that the elongation or the flattening does not greatly change the emission from any point on the atmosphere limb, then in both cases one would expect the limb flux from the long edge of the distorted atmosphere to dominate the limb flux from the short edge. Recalling the discussion about the alignment of polarization of flux emitted by an atmosphere surface, one expects the polarization of the limb flux to align with the long axis of the projection. Now the flux from the photodisk center of the spherically symmetric atmosphere will be unpolarized. When the elongation or flattening occurs, the radiation field incident on the photodisk center plausibly becomes stronger in the stretched direction. The nature of Rayleigh-type scattering then implies that the polarization of the flux from the photodisk center will be aligned perpendicular to the long axis of the distorted atmosphere. The simple physical picture is only plausible. However, as shown in § 4, the polarization alignment behavior of the flux from the realistic model (see § 3.3) does agree with that of the simple physical picture. Clearly, the heuristic model does not agree with the simple physical picture. Provided that the emitted l flux is never greater than the emitted r flux for the spherically symmetric model, it is impossible for the heuristic model polarization alignment to vary at all; as stated above, this alignment is always with the long axis of the heuristic model. The importance of the distinction in the polarization alignment behavior between the heuristic and realistic models is investigated in § 4.

As a last point, it should be noted that equation (14) is an exact formula for the polarization of the net flux from a spherically symmetric atmosphere that has a sector of its projection covered by an opaque screen. For this interpretation of equation (14), in equations (13a) and (13b) the g variable has to be regarded as the radius variable of the spherically symmetric atmosphere's projection, and the factor ac must be set to 1. The relationship between the parameter c/a and the angle θ_s of the visible sector of the spherically symmetric atmosphere's projection is given by

$$\frac{1 - c/a}{1 + c/a} = \frac{\sin \theta_s}{\theta_s} \quad \text{or} \quad \frac{c}{a} = \frac{\theta_s - \sin \theta_s}{\theta_s + \sin \theta_s} . \tag{16}$$

The position angle of polarization of the flux from the visible sector is aligned perpendicular (parallel) to the bisector of the visible sector when $\theta_s < \pi$ ($\theta_s > \pi$) provided that $F_l < F_r$.

3.3. *The Realistic Model*

The realistic model is obtained by distorting the spherically symmetric model into an axisymmetric ellipsoidal model. The surfaces of constant density, the photosphere, and the core of the realistic model are all made to be geometrically similar surfaces. The ratio of the polar semiaxis to the equatorial semiaxis of the model, c/a, and the angle of inclination of the polar axis of the model to the line of sight are free parameters. When the inclination angle is set to 90°, the polarization of the net flux is maximized for a given c/a value. When the inclination angle is 0°, the polarization of the net flux is always 0%, since the model is circularly symmetric about the line of sight in this case. Other parameters of the realistic model are the equatorial $r_{\rm ph}$, $r_{\rm core}$, R, and $v_{\rm ph}$.

An ellipsoidal coordinate is defined by

$$g = [(x/a)^2 + (y/a)^2 + (z/c)^2]^{1/2} , \tag{17}$$

where x and y are the equatorial plane coordinates, z is the polar coordinate, and a and c are the equatorial and polar semiaxes of the photosphere, respectively. Of course, a and the equatorial $r_{\rm ph}$ are the same quantity. For the realistic model calculations reported in § 4, the homologous density distribution is chosen to be an inverse power law of g.

Note that radial continuum optical depths to any surface of constant g, such as the photosphere and core, are functions of the angle between the radius direction and the polar axis. For example, the ratio of the polar radial optical depth to the equatorial radial optical depth for a surface of constant g is c/a. A procedure that would be consistent with the assumed homologous density distribution would be to find surfaces where the angle-averaged optical depth to a point on each surface is a constant for that surface. The photosphere and core could then be chosen from these surfaces of constant angle-averaged optical depth. Since the assumed model is highly parameterized, such a consistent procedure would be pointless. It is just assumed that the physical conditions are such that the photosphere and core are surfaces of constant g. The equatorial radial optical depths to the photosphere and the core are used as the optical depth parameters of the realistic model. To be consistent with the spherically symmetric and heuristic model parameters, the equatorial radial optical depths to the photosphere and core are simply denoted by $\tau_{\rm ph}$(con) and $\tau_{\rm core}$(con), respectively.

Since polarization is calculated from the difference of two always positive Stokes parameters, and flux from their sum, it is clear that obtaining numerically accurate converged polarization spectra is going to be more difficult than obtaining

comparably acceptable flux spectra. This difficulty increases as polarization decreases. In numerical experiments with the realistic model and the DCO approximation, it has been found that to obtain a synthetic polarization spectrum with a wavelength band of about 1000 Å and a numerical uncertainty of order 0.2% in polarization required typically 5–20 hr of VAX 11/780 CPU time. This conclusion is, of course, dependent on the computer program used for the calculations. The computer program used for all the calculations reported in this paper is called S7. An early version of S7 is listed in SPM I (p. 276). To obtain significantly better numerical accuracy than 0.2% in the calculations would require exorbitant computational time and/or an improved version of S7. Thus, no attempt was made to reduce the uncertainty below 0.2% in calculations for the realistic model synthetic polarization spectra displayed in § 4. An investigation of the inaccuracies introduced by the 0.2% uncertainty showed that they are mainly quantitative, not qualitative. The important polarization features in the SN 1987A spectropolarimetric data range in size from ~0.1% to ~4% and are typically of order 1% or less (Cropper et al. 1988; Schwarz 1987b; Jeffery 1991). Thus, a numerical uncertainty of 0.2% is uncomfortably large. Given the numerical uncertainty problem and the computational demands of realistic model calculations, it was decided to defer synthetic spectrum-fit calculations with the realistic model to future research. For the present paper, the realistic model was used only in the demonstration calculations in order to show the realistic model spectrum behavior and to compare this behavior with heuristic model spectrum behavior (see § 4). The heuristic model is used for the synthetic spectrum-fit calculations reported in § 6.2. Heuristic model calculations take roughly two orders of magnitude less time than realistic model calculations. The numerical inaccuracy of heuristic model calculations is usually negligible. The reason for the relatively high accuracy of the heuristic model calculations is that the relative difference of the F_l and F_r fluxes in equation (14) for the heuristic model polarization is usually much larger than 0.2%.

4. DEMONSTRATION RESULTS

This section presents some demonstration results of synthetic spectrum calculations and compares the behaviors of spectra calculated with the two aspherical models. The homologous density distribution was chosen to scale with an inverse power law of the radius for the spherical and heuristic models and with an inverse power law of the g parameter (see § 3.3) for the realistic model. The index of the inverse power law is denoted by n. Given an inverse power law scaling function, equation (4) for the Sobolev optical depth of a pseudoline can be rewritten as

$$\tau(r) = \frac{\Delta\lambda}{\lambda_{ps}} \frac{c}{|dv/ds|} \frac{\tau_{ph}(\mathrm{con})(n-1)/r_{ph}}{1-(r_{ph}/R)^{n-1}} \left(\frac{r_{ph}}{r}\right)^n , \qquad (18)$$

and using equation (7), an analytic solution for r_{core} is found to be

$$r_{core} = r_{ph}\{[\tau_{core}(\mathrm{con})/\tau_{ph}(\mathrm{con})][1-(r_{ph}/R)^{n-1}] + (r_{ph}/R)^{n-1}\}^{-1/(n-1)} . \qquad (19)$$

The first demonstration calculation was done to verify the DCO approximation in a particularly extreme case of the spherically symmetric model. The index of the inverse power law was chosen to be 10^4, and the continuum optical depth to the core was set to 5. The ratio of the core radius to the outer cutoff radius of the atmosphere was 0.9999254. The density of pseudolines was chosen sufficiently high to eliminate all apparent finite wavelength increment behavior. The atmosphere approximated by this spherically symmetric model case is a semi-infinite plane-parallel electron scattering atmosphere. The specific intensity emergent from the atmosphere divided by the astrophysical flux (the conventional physical flux divided by π) and the polarization of this specific intensity are plotted as functions of μ (the cosine of the angle between the normal to the atmosphere surface and the emergent specific intensity beam direction) in Figure 3. Also plotted in Figure 3 are the exact results for the semi-infinite plane-parallel electron scattering atmosphere given by Chandrasekhar (1960, p. 248). The agreement between the DCO approximation results and the exact results is satisfyingly close.

The semi-infinite plane-parallel scattering atmosphere is actually not a strongly polarizing atmosphere. In general, the more extended a scattering atmosphere (i.e., the larger the spatial width of the atmosphere is relative to the characteristic length scale of the whole radiating body), the greater is the atmosphere's polarizing power. The simplest way to see this is to consider the radiation field convergent on a scatterer on an atmosphere's surface. In a plane-parallel case all the beams convergent on this scatterer originate infinitely far away in the atmosphere. In the extended-atmosphere case, some of the

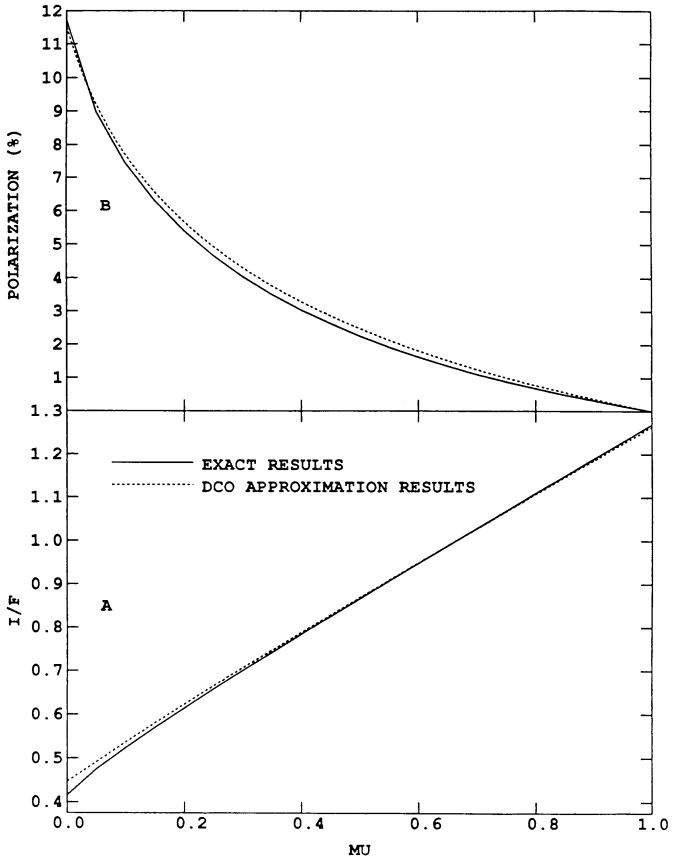

FIG. 3.—Exact and DCO approximation results for the emergent specific intensity and its polarization for the semi-infinite plane-parallel electron scattering atmosphere. F is the astrophysical flux (the conventional physical flux divided by π), and μ is the cosine of the angle between the normal to the atmosphere surface and the direction of the emergent specific intensity beam.

convergent beams can start no farther away than the outer edge of the atmosphere. (Note that beams originating in the thermalization layer are considered to have started infinitely far away in this argument.) One would expect there to be a tendency for the convergent radiation field in a less extended atmosphere to be more isotropic than in a more extended atmosphere. The more isotropic the incoming radiation field is, the more polarization cancellation there is in the outgoing scattered radiation field. This effect of extension is confirmed by comparison of the Chandrasekhar plane-parallel electron scattering atmosphere results to the results of Cassinelli & Hummer (1971) for extended spherically symmetric electron scattering atmospheres. For example, in the Cassinelli & Hummer results, the extreme limb polarization goes to 100%, not 11.7% as in the Chandrasekhar results. The extension of a non–plane-parallel atmosphere clearly increases as the density distribution is made to decrease less steeply with radius.

The remaining demonstration results were calculated to investigate the behavior of the line and continuum polarization of the flux emergent from the realistic and heuristic models. The model parameters for the calculations are given in Table 1. The line that was chosen for this investigation is the Hα line, which has an E_1 coefficient of 0.346. The photospheric Sobolev optical depth of this line was set to 300 in all cases; this value is typical of values of the Hα line photospheric optical depths that were found satisfactory by JB for fitting the observed SN 1987A Hα P Cygni line trough. As noted in § 3.1, the Hα line profiles in SN II flux spectra typically show net emission, and thus the real SN II Hα line is not well approximated as a pure resonance scattering line. This being the case, the Hα line in the demonstration calculations can be regarded simply as a representative strong pure resonance scattering line with a relatively large intrinsic polarizing effect.

The inclination angle was set to 90° for all the realistic model calculations. If the inclination angle of the realistic model were chosen to be oblique, then a redshift of the maximum of the flux emission feature from the line-center wavelength would occur (see SPM I, Figs. 4.8*a* and 4.13*a*, and JB, Fig. 9). Such a redshift would probably be the most noticeable effect of an oblate or prolate asymmetry on a flux spectrum. Non-Sobolev effects can cause redshifts in spectra from spherically symmetric atmospheres (see, e.g., Hamann 1981). However, these non-Sobolev redshifts are due to the characteristic random velocity v_{ra}. If v_{ra} is due purely to thermal motions, then it can only be of order 10 km s^{-1}, since supernova temperatures are of order 10^4 K. Redshifts corresponding to much higher velocities may indicate asymmetry or random motions with much higher than thermal velocities. There is another redshifting effect that can operate in the nebular phase of a supernova: redshifts due to electron scattering of line-emitted photons. This latter effect probably occurred in SN 1987A (see the discussion in § 6.1).

The logarithmic flux spectra are displayed in the figures for the aspherical models. Using the logarithmic flux spectra is convenient for checking for flux spectrum convergence when using the DCO approximation, since, as discussed in § 2, convergence is obtained when the flux spectrum stops changing except for an overall scale factor. Instead of showing polarization in the figures, the fractional Q parameter is shown. The fractional Q and U parameters are the conventional Stokes Q and U parameters divided by the total flux and multiplied by 100%. Since the models used for the calculation are axisymmetric, the fractional U parameter is everywhere zero when the l and r-axes are chosen to align with the polar and equatorial axes of the model; this choice of axes is made throughout this section. The absolute value of the fractional Q parameter is the polarization; positive fractional Q parameter means that the polarization is aligned with the polar axis, and negative fractional Q parameter means that the polarization is aligned with the equatorial axis. The fractional Q parameter scale in the figures was made to increase downward, since this seemed to give a nicer presentation.

The flux and fractional Q-parameter profiles displayed in Figure 4 were calculated without continuous opacity. (The photospheric radius is defined to be the same as the core radius when there is no continuous opacity.) Thus, the polarization is entirely due to the intrinsic line polarizing effect. The line opacity was scaled with an inverse power law with index 12; this index is rather large, and so this case has a geometrically thin atmosphere. The c/a parameter was set to 0.8 for both the realistic and heuristic models. This choice gives an oblate asymmetry. For the heuristic model there is, of course, neither real oblateness or prolateness; there is only an elliptical projection asymmetry such that $c/a = 0.8$ gives results identical to those given by $c/a = 1.25$, except for a shift of 90° in the position angle of polarization (see eqs. [14] and [15]). The flux spectra of the realistic and heuristic models are in very close agreement. The heuristic model flux spectrum is, of course, exactly a spherically symmetric model flux spectrum. The close agreement of the two flux spectra shows that even large shape asymmetry is probably hard to detect from an examination of a flux spectrum, unless there are significant redshifts of the

TABLE 1

PARAMETERS OF THE ASPHERICAL MODEL DEMONSTRATION CALCULATIONS

Figure	n	v_{ph} (km s^{-1})	r_{core}	R	τ_{core}(con)	X_{ph}	Number of Pseudolines	Model
4	12.0	15000	1.000	2.5	0.0	...	0	Re
4	12.0	15000	1.000	2.5	0.0	...	0	He
5	12.0	15000	0.905	2.5	3.0	0.15	70	Re
5	12.0	15000	0.905	2.5	3.0	0.05	206	He
6	4.5	4000	0.732	3.5	3.0	0.3	60	Re
6	4.5	4000	0.732	3.5	3.0	0.15	95	He

NOTE.—The abbreviations Re and He stand for realistic model and heuristic model, respectively. For the demonstration calculations $c/a = 0.8$, $r_{ph} = 1$, τ_{ph}(con) = 1 (for those cases with continuous opacity), the photospheric Hα Sobolev optical depth τ_{ph}(Hα) is equal to 300, E_1(Hα) = 0.346, the continuum radiation field emergent from the core is wavelength-independent, and the inclination angle for all the realistic model calculations was set to 90°. For the realistic model cases, v_{ph}, r_{core}, R, and τ_{core}(con) are all equatorial quantities.

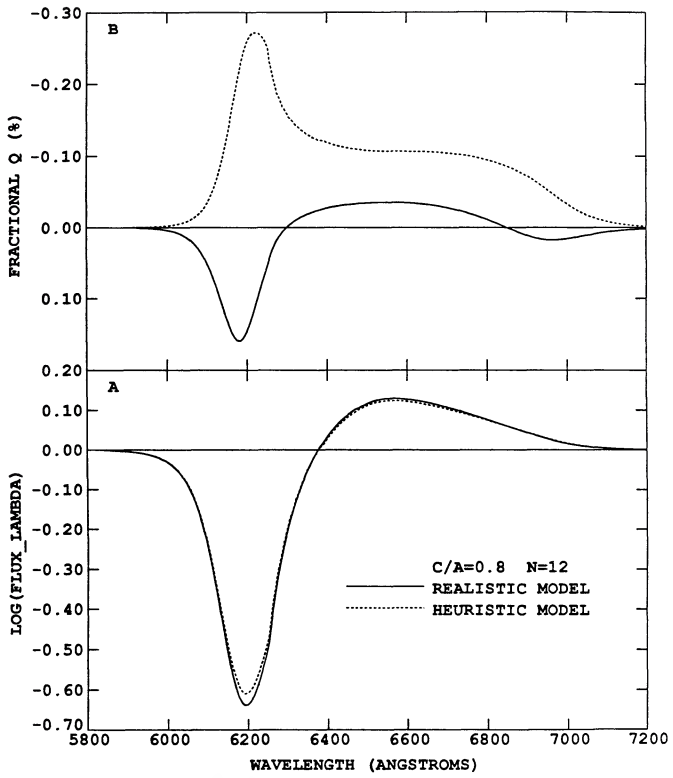

FIG. 4.—Flux and fractional Q-parameter line profiles calculated for the heuristic and realistic models. No continuous opacity was included in the calculations for these profiles. The n parameter is the index of the inverse power law that was used as the scaling function for the opacities.

maxima of the flux emission features that can be attributed to shape asymmetry and an oblique inclination angle. This conclusion is confirmed by the results presented below in this section and in SPM I and SPM II.

The behaviors of the fractional Q-parameter profiles for the realistic and heuristic models in Figure 4 are quite distinct. The realistic model fractional Q parameter shows changes in sign, which, of course, means that the realistic model polarization shows shifts of 90° in position angle. The positive Q flux comes from scattering from the front and rear of the atmosphere. ("Front" and "rear" in this paper mean those atmosphere regions roughly nearer and farther, respectively, from the observer than the photosphere.) The positive Q-flux polarization is, of course, aligned with the short axis of the projection of the model. The explanation of the 90° position-angle shift between limb- and front-scattered flux is given in the discussion in § 3.2. The 90° position-angle shift between the limb- and rear-scattered flux has essentially the same explanation. The heuristic model polarization should not, of course, show any position-angle shifts and is expected to align with the long axis of the model (see § 3.2). The behavior of the heuristic model fractional Q parameter is consistent with these expectations.

The size of the polarization features of both models is easily understood. There is a relatively large amount of polarized flux scattered from the limbs of the atmospheres; this flux gives rise to the polarization near the line-center wavelength. There is less polarized flux scattered from the front and rear. However, the front-scattered flux is less diluted by unscattered, unpolarized photospheric flux due to the scattering out of the line of sight of this photospheric flux. Thus, there are polarization maxima at wavelengths near the minima of the flux spectra. At wavelengths near and redward of the line-center wavelength, most or all of the observer-directed photospheric flux never intersects a CD velocity surface and so escapes the atmosphere without being scattered. Thus, the limb- and rear-scattered fluxes are more highly diluted than the front-scattered flux. The size scales of the polarizations for the realistic and heuristic models do not agree. Since the models are quite distinct, this is not a surprising result. It should be remarked that the numerical accuracy of the realistic model calculation in his case is of order 0.01% in polarization. A much better numerical accuracy than 0.2% could be achieved in this case because only a single line was included in the calculation.

Figure 5 displays the results of calculations that are identical to the calculations done for Figure 4, except that electron opacity has been included and, consequently, the core radii of the models are smaller. The core continuum optical depth for both models was set to 3. The small regular oscillations seen in the realistic model flux and fractional Q-parameter spectra are a consequence of the finite wavelength increment between the pseudolines. The density of pseudolines in the heuristic model calculation was 3 times that in the realistic model calculation, and thus the oscillations are unnoticeable in the heuristic model spectra. The flux spectra from the two models are again very similar. There is an overall scale difference, but this is just a consequence of the different density of pseudolines used (see § 2). The fractional Q-parameter spectra (essentially the polarization spectra) of the two models are qualitatively similar, in contrast to the case without continuous opacity. This simi-

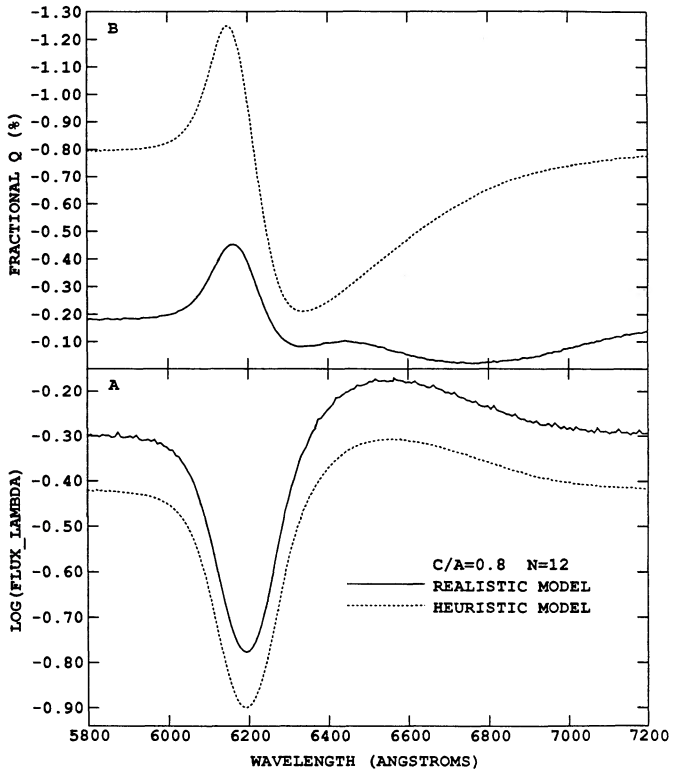

FIG. 5.—Flux and fractional Q-parameter line profiles calculated for the heuristic and realistic models with continuous (electron-scattering) opacity included in the calculations.

larity is a consequence of the fact that the geometry of the two models and the radiative transfer of the limb flux (see below) is such that the polarization behavior of this limb flux is much the same in both models. As Figure 4 demonstrates, the different geometry of the two models leads to different polarization behaviors for flux scattered from the front and rear of the two models. However, when electron-scattering opacity is present, limb flux can appear at all wavelengths. The quantity of limb flux is sufficient that the overall polarization behavior seen in Figure 5 is dominated by the limb flux.

The formation of the polarization spectra in Figure 5 is easily understood. Far from the line-center wavelength there is effectively no line opacity, and a continuum polarization appears due to electron-scattered flux mostly from the limb. Near the line-center wavelength, the line scatters into the line of sight photons that would never have been scattered into the line of sight without the line and photons that have previously been scattered into the line of sight by electron scattering. Although the line is intrinsically polarizing, its polarizing effect is much less than that of electron scattering. Thus, both sets of photons that the line scatters into the line of sight from the limb lead to a decrease in polarization near the line-center wavelength relative to the continuum polarization level. In front of the photosphere, the line scattering, as discussed above, reduces the diluting effect of the unpolarized photospheric flux by scattering it out of the line of sight. With this diluting effect reduced, the polarization chiefly due to the flux scattered from the limbs by the electrons is enhanced, and thus a polarization maximum associated with the line-flux profile trough is formed.

Figure 6 shows realistic and heuristic model results of calculations with electron opacity and an inverse power law index of 4.5. Again, the core continuum optical depth for both models was set to 3. The small oscillations seen in the realistic model spectra are again due to the finite wavelength increment used for the pseudolines. For an atmosphere with an index 4.5 and with a line of photospheric Sobolev optical depth 300, an outer cutoff radius of 3.5 is not effectively an infinite radius. This explains the rather steep blue edges of both the flux and polarization line trough features. The flux and fractional Q-parameter spectra of Figure 6 can be given essentially the same explanation as those of Figure 5. However, since an atmosphere with an index of 4.5 is more extended than one with an index of 12, one expects generally higher polarizations from the Figure 6 models than from the Figure 5 models. The generally higher polarization given by the Figure 6 heuristic model and the higher polarization maximum given by the Figure 6 realistic model are consistent with this expectation. However, the continuum polarization of the Figure 6 realistic model is not significantly higher than the continuum polarization of the Figure 5 realistic model. The reason for this is probably just the numerical uncertainty of the realistic model calculations; from § 3.3 recall that this uncertainty is $\sim$0.2%. Also on account of the numerical uncertainty, it is not known whether the positive regions in the Figure 6 realistic model fractional Q-parameter spectrum are significant.

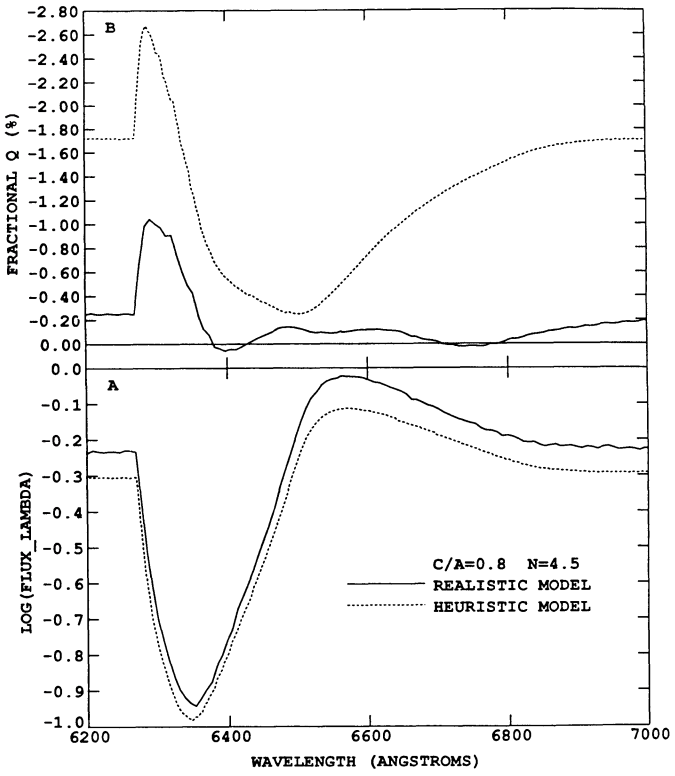

FIG. 6.—Same as Fig. 5, but for a different set of model parameters (see Table 1).

If a core continuum optical depth of 10 had been used for the heuristic model calculations for Figures 5 and 6, changes of order 0.2% would occur in the fractional Q-parameter spectra. If the intrinsic line polarizing effect had been turned off in the calculations for Figures 5 and 6, the effect on the polarization spectra is about what one would expect from a comparison of these figures with Figure 4: in the heuristic model polarization spectra, the polarization in the line region would decrease by an amount of order 0.1%–0.2% in the central region of the line profile, and there would be a declining decrease as one moved away from the central region; in the realistic model polarization spectra, the polarization associated with the line trough would be enhanced and the polarization near the line-center wavelength would be decreased by amounts of order 0.1% (see, e.g., SPM II, Figs. 9 and 10). The conclusion drawn is that the intrinsic line polarizing effect is not quantitatively insignificant, but that it will be of secondary importance for almost all lines during the photospheric phase whenever a realistic electron scattering opacity distribution is included in the atmosphere. This conclusion is confirmed by all the numerical experiments that have been done with $\tau_{\rm core}(\rm con) \gtrsim 1$. The conclusion is welcome because, as discussed in § 2, the Sobolev-P method can only be expected to treat the intrinsic line polarizing effect qualitatively, and it is not clear a priori that the intrinsic line polarizing effect is operative to any significant degree in supernova atmospheres.

An unwelcome conclusion drawn from the analysis of the demonstration results is that the explanation for the basic shape of fractional Q profiles shown in Figures 5 and 6 is not strongly dependent on the nature of the asymmetry of the models. Therefore, polarization behavior associated with a P Cygni line profile can be expected to have a characteristic profile (polarization minimum associated with the flux emission feature and polarization maximum associated with the flux trough feature) for a broad range of possible asymmetries. The mere observation of this characteristic polarization profile will not by itself give much information about the nature of the observed supernova's asymmetry. For example, the character-

istic polarization profile will not show whether the supernova is axisymmetric or not. The position-angle spectrum may yield more immediate information about the nature of the asymmetry. If the position angle is constant with wavelength except for shifts of 90°, this would be consistent with an axisymmetric asymmetry. It should be noted, however, that constancy of position angle does not in itself prove axisymmetry. The position angle would stay constant without axisymmetry if all the polarized fluxes contributed by different regions of the atmosphere and individually fixed position angles and a constant ratio with wavelength. Such a constant ratio would be hard to arrange with an opacity that was strongly wavelength-dependent. However, with wavelength-independent electron scattering a constant ratio is easier to imagine. Line scattering opacity, because of its wavelength dependence, could clearly lead to wavelength variation in the position angle in non-axisymmetric cases by varying the relative amounts of polarized flux contributed from different regions as wavelength varied. Thus, if the position angle observed for a supernova was constant (except for 90° shifts) for the line polarization profiles as well as for the continuum polarization, there would be a strong case for an axisymmetric asymmetry.

Further demonstration results can be found in SPM I and SPM II. In SPM I (p. 110), a catalog of oblate and prolate realistic model spectra calculated without continuous opacity is given. In SPM II, realistic model spectra calculated both without and with continuous opacity are reported. Also reported in SPM II are results that give further verification that the DCO approximation can be made quantitatively accurate.

5. THE INTERSTELLAR POLARIZATION CORRECTION AND OTHER CORRECTIONS FOR THE SN 1987A DATA

A priori, a significant interstellar polarization (ISP) in the direction SN 1987A must be expected. Galactic foreground ISP for the region where SN 1987A is located has been found by Schmidt (1976) to be 0.40% ± 0.13% at position angle 20°. In the LMC most of the significantly polarized stars with polarization due to LMC ISP lie in the 30 Doradus region, where SN 1987A is located; the polarization of these stars due to LMC ISP ranges at least as high as 4% (Clayton, Martin, & Thompson 1983, hereafter CMT). Stars within ~15′ of SN 1987A have LMC ISP of order 1% (Cropper et al. 1988). To obtain intrinsic polarization, the ISP must be "subtracted" off. The actual correction procedure requires that the ISP fractional Q and U parameters be subtracted from the observed fractional Q and U parameters in order to obtain intrinsic fractional Q and U parameters (see, e.g., Martin 1974). The intrinsic polarization and position angle are then obtained using the fractional Q and U parameters and, *mutatis mutandis*, equations (2) and (3). Since the observed SN 1987A broad-band polarization is of order 1% or less (e.g., Barrett 1988) and significant line polarization features in the observed SN 1987A spectropolarimetric data range from ~0.1% to ~3% (Cropper et al. 1988), it is clear that the observed polarization behavior will be a greatly distorted version of the intrinsic polarization behavior unless the SN 1987A ISP is unexpectedly small. A particularly unwelcome effect is that bumps (dips) in the intrinsic polarization spectra can give rise to dips (bumps) in the observed polarization spectra. Clearly, analyses of the SN 1987A polarimetry that are better than very qualitative require fairly accurate knowledge of the SN 1987A ISP.

Méndez (1990), in a private communication, describes broad-band polarimetry of SN 1987A taken at the La Plata Observatory during the period of late 1988 and earlier 1989. These observations show a polarization spectrum that is consistent with a Serkowski law spectrum for interstellar polarization and that is unvarying over a 6 month period. The Serkowski empirical ISP law is given by

$$P = P_{\max} \exp\left[-K \ln^2(\lambda_{\max}/\lambda)\right] \quad (20)$$

(see, e.g., Serkowski 1973). For the La Plata SN 1987A polarization spectrum, Méndez reports that $P_{\max} \sim 1.05\%$, $\lambda_{\max} \sim 5400$ Å, $K \sim 1.1$, and the position angle is ~34°. The reported value of $\lambda_{\max}$ is consistent with the ranges of 4500–5500 Å and 5100–6500 Å reported by CMT for the foreground Galactic ISP and the LMC ISP, respectively. The reported K and $\lambda_{\max}$ values are not quite consistent with the empirically determined Galactic relation

$$K = (1.86 \pm 0.09)\lambda_{\max} - (0.10 \pm 0.05) \quad (21)$$

(Wilking, Lebofsky, & Rieke 1982), where $\lambda_{\max}$ is measured in microns. This relation may, of course, need to be modified for the LMC. The constant position angle of the La Plata SN 1987A polarization spectrum is consistent with what one expects for an ISP spectrum (e.g., CMT). Both the shape of the reported La Plata SN 1987A polarization spectrum and its time independence argue for the hypothesis that this spectrum is due entirely to ISP. That the intrinsic SN 1987A polarization would have vanished by about day 650 (approximately the epoch of the La Plata observations) should not be unexpected. Sometime of order day 300, the electron opacity optical depth to the center of the ejecta should have fallen to less than 1 (see, e.g., Axelrod 1988; see also the discussion in § 6.1), and the supernova will have entered the nebular phase (see § 3.1). Therefore, by about day 650, it is plausible that the electron opacity optical depth through the ejecta has fallen to much less than 1. With such a low electron opacity optical depth, little flux will be scattered by electrons and the electron polarizing effect will vanish. The line profiles by day 650 are almost pure emission profiles (see, e.g., Phillips et al. 1990, Fig. 6). Thus, most of the line photons that emerge from line resonance regions will have originated in those resonance regions and will escape the ejecta without scattering again; the energy for the line photons is probably mostly due to the decay of radioactive matter in the ejecta (e.g., Axelrod 1988). Some of these line photons may be scattered and polarized by the line itself in their resonance region of origin. However, the resonance regions are probably small enough to be quite homogeneous and isotropic, and thus the net flux emergent from them should be unpolarized. Therefore, even if the intrinsic line polarizing effect is operative on about day 650, it will probably not contribute to the polarization of the net supernova flux. The strength of all these arguments makes it probable that the La Plata SN 1987A polarization spectrum is in fact the SN 1987A ISP, and therefore this spectrum (in a Serkowski law parameterized form) has been adopted for correcting the SN 1987A polarimetric data displayed in § 6.2. Figure 7 displays the wavelength variation of the adopted ISP and of its fractional Q and U parameters.

It should be remarked that any contamination of the La Plata observations of SN 1987A by light from other field stars, especially stars 2 and 3, would not alter the argument that the La Plata spectrum is the SN 1987A ISP provided that all the light sources were unpolarized and the ISP was constant over the field of observation. (Stars 2 and 3 are within 3″ of SN 1987A; e.g., White & Malin 1987.)

In addition to correcting for the ISP, the polarimetry dis-

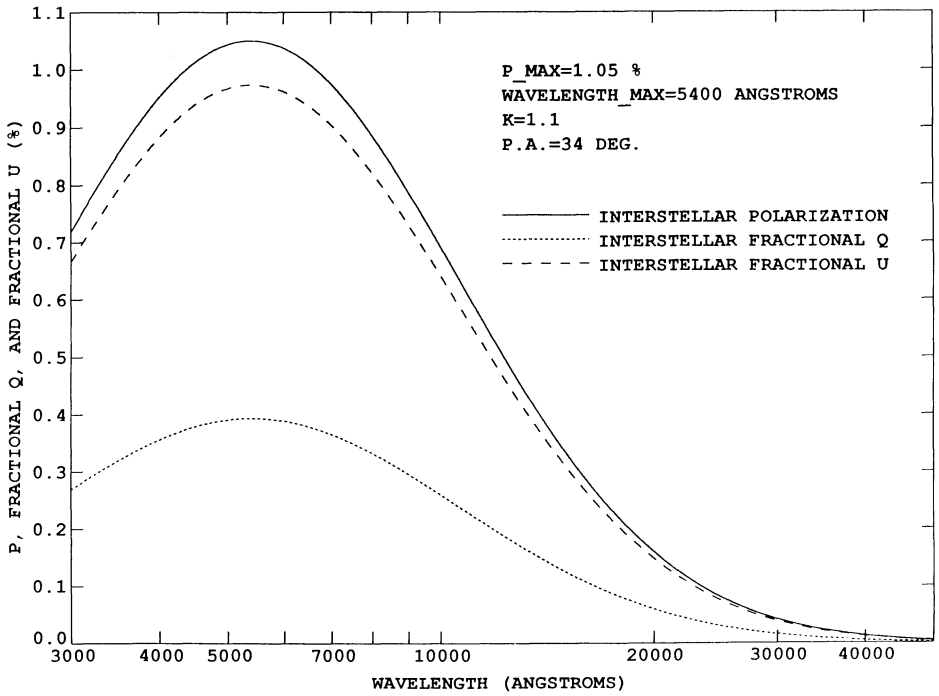

FIG. 7.—Wavelength variation of the adopted SN 1987A interstellar polarization and interstellar fractional Q and U parameters

played in § 6.2 is also corrected for the redshift due to the radial velocity of SN 1987A with respect to the Sun. The value of the radial velocity used is 286 km s^{-1}, which has been determined by Wampler & Richichi (1989) from circumstellar lines. The displayed flux spectra are also corrected for the redshift due to the radial velocity. Additionally, the flux spectra are corrected for interstellar reddening using the $E(B-V)$ value 0.17 reported for the field of SN 1987A by Walker & Suntzeff (1990) and the interstellar reddening law given by Code et al. (1976). The highest flux on every figure is normalized to 1.

6. OBSERVATIONS, SYNTHETIC SPECTRA, AND THE ASYMMETRY OF SN 1987A

6.1. *Summary of the Evolution of the SN 1987A Polarization*

Although this paper is primarily concerned not with the evolution of the SN 1987A polarization but rather with the synthetic-spectrum analysis of some of the continuum and line polarization data, it is useful to summarize this evolution and give an interpretation in order to help establish the context of the analysis. From the remarks made in § 5, it is clear that the summary will be very dependent on the ISP correction adopted. The corrected data referred to here are presented in a catalog of SN 1987A corrected polarimetry given by Jeffery (1991). This catalog uses the same ISP and radial velocity corrections adopted in this paper and covers the period from day 2 through day 262. The catalog includes broad-band data (taken from Cropper et al. 1987; Rao et al. 1987; Schwarz 1987b, c; Bailey, Ogura, & Sato 1987; Magalhaes & Velloso 1987; Barrett 1988; Clocchiatti & Marraco 1988; Bailey 1988; Méndez et al. 1988), narrow-band data (taken from Schwarz 1987b, c), and spectropolarimetry (reported by Cropper et al. 1988). The three U-band observations given by Benvenuto et al. (1987) are omitted from consideration; these observations taken at the La Plata Observatory were not included in the collection of La Plata broad-band observations reported by Méndez et al. (1988), and two of these U-band data are quite inconsistent, by being too large in uncorrected form, with other U-band observations taken from near the same epochs (see, e.g., Barrett 1988, Table 1A).

The broad-band *UBVRI* polarizations are in the range 0.1%–0.4% on day 2. Subsequently, there is a general trend upward until about days 30–40, when the polarizations in all five bands are of order 0.5%. From about day 40 to day 80, the U and V polarizations tend downward and finish by being of order 0.1%–0.4%; the B and RI polarizations in this period do not show a clear upward or downward trend. After day 80, the broad-band polarimetry of which the author is aware becomes much less abundant. The sparse broad-band data can be supplemented with broad-band polarizations estimated from the continuum polarization levels of the spectropolarimetry taken in the days 100–135 epoch. However, even with this extra information, no clear trends can be identified. What can be said is the observations are consistent with all *UBVRI* polarizations being roughly of order 0.5% or higher in the days 80–262 epoch. All the *UBVRI* bands exhibit isolated data points of order 1% or higher; the highest broad-band polarization is $\sim$1.5% in the V band on day 144. On day 262, the *UBVRI* polarizations were about 0.6%, 0.2%, 0.5%, 1%, and 0.7%, respectively.

There are sets of *JHK* data for days 2, 26, and 262. The *JHK* polarizations for days 2 and 26 agree roughly with the *UBVRI* polarizations from the same epochs. The day 262 *JHK* polarizations are about 1.2%, 1.6%, and 1.7%, respectively. The sole published L polarization, also for day 262, is about 1.6%.

The position-angle behavior of the broad-band polarizations is rather consistent. About 80% of the position angles lie in the 100°–130° range. (Position angle is measured clockwise from north.) Only in the U band are as many as about 40% of the points outside this range. Only about 5% of the data points differ from the 100°–130° range by more than about 20°. The

continuum polarization position angles from the spectropolarimetry are consistent with the 100°–130° range in 11 out of 14 cases. There is no epoch when the broad-band and continuum position angles do not seem to favor the 100°–130° range.

The catalog spectropolarimetry and narrow-band polarimetry span the days 4–162 epoch. Of order 20 line polarization profiles seen in these data conform to the characteristic polarization profile identified in § 4. Some line polarization profiles clearly do not conform to the characteristic profile, and in other cases line blending makes classification difficult. On the whole, the observations confirm the explanation of line polarization profile formation outlined in § 4. The line position-angle profiles often showed shifts from the continuum position angle. These shifts ranged from 0° to 90° without any obvious favored value.

There are spectropolarimetric observations for days 315 and 350 reported by Bailey (1988, hereafter B88). These observations were not available for the catalog. The continuum polarization and position angle of B88's data would be roughly of order 0.5%–1% and 110°, respectively, if they were corrected using the La Plata ISP. The ISP estimate B88 adopts is sufficiently similar to the La Plata ISP that his ISP–corrected polarization spectrum for day 350 (his Fig. 6) is probably very similar to what would have been obtained if the La Plata ISP had been used for the correction, except for an overall additive constant. The polarization behavior associated with the line flux profiles in this spectrum is rather different from the characteristic polarization profile. This is perhaps to be expected; the characteristic polarization profile was associated with P Cygni flux profiles; the line flux profiles associated with the polarization profiles in B88's spectrum are emission-line profiles. (The days 315–350 epoch is in a postphotospheric phase, but it is not likely to be in the full nebular phase [see below].) In B88's polarization spectrum there are polarization minima associated with the center of the flux emission features and polarization maxima associated with the red wings of the flux emission features. B88's plot of polarized intensity (his Fig. 7) for day 350 shows polarized intensity bumps associated with the line flux emission features. These bumps are broader and somewhat redshifted from the line flux emission features. Clearly, the polarization minima associated with the center of the line flux emission features are not due to lack of polarized flux relative to the continuum amount of polarized flux, but rather are due to a large dilution by unpolarized line emission flux. The line position-angle profiles show shifts from the continuum position angle of only about 20° or less.

An interpretation of the intrinsic SN 1987A polarization evolution is as follows. Up until at least day 200, NLTE calculations (Höflich 1988) suggest that the electron opacity optical depth through the ejecta is much greater than 1; from the discussion given in § 4, it then follows that the polarization in this period is mainly due to electron scattering. An argument given below suggests that electron scattering is still the dominant source of polarization at and after day 350. Therefore, the polarization at all times is probably due mainly to electron scattering; the intrinsic line polarizing effect is probably only of secondary importance at most. In the first few days polarization is relatively low. However, this does not necessarily mean that the outer ejecta is relatively less asymmetric than the inner ejecta. The outer density gradient of the ejecta is expected to be rather steep; the JB homologous density distribution in the outer ejecta can be approximated by an inverse power law with index of order 12–13. The steep gradient causes the atmosphere to be rather like a plane-parallel atmosphere and therefore to have relatively low polarizing power (see § 4). Shapiro & Sutherland (1982) calculated continuum polarization for axisymmetric ellipsoidal atmospheres that emitted at each surface point like Chandrasekhar's plane-parallel electron scattering atmosphere (see § 4). From their results and the early broad-band polarimetry one would estimate that SN 1987A had a length-width difference of order 20%. After the first few days the supernova photosphere receded into ejecta where the density gradient was shallower. Thus, the atmosphere became more extended and its polarizing power increased. This explains the increase in polarization up until about day 40. After day 40, there appears to be no immediate simple explanation for the course of the polarization evolution. The relatively high polarizations (i.e., ~ 1 or higher) that appeared in some bands after about day 100 may be due to a further decrease in density gradient near the photosphere that may have occurred about day 100 (see JB, Figs. 16 and 18*a*). This interpretation does not explain why other band polarizations from the post–day 100 epoch were much lower (i.e., ~ 0.5 or lower).

The behavior of the position-angle data shows that SN 1987A had a special axis throughout at least the first 350 days at of order 115°. The existence of this special axis is consistent with the hypothesis that SN 1987A had an axisymmetric component to its asymmetry. However, the fact that there was some variation in the broad-band position angles and strong variation in the line position-angle profiles shows that the asymmetry cannot be purely axisymmetric. The variation of the line position-angle profiles is discussed further in § 6.2.

After day 350, the author is not aware of any further polarimetric observations except for yet unpublished La Plata observations discussed by Méndez (1990). In the time between day 350 and day 550 there is, however, indirect evidence of significant electron scattering, and thus evidence that the full nebular phase had not yet begun. Many, but not all, prominent emission-line features in this period had redshifts from their line-center wavelengths in the local SN 1987A frame (see, e.g., Witteborn et al. 1989; Phillips et al. 1990). In the period from about day 550 to day 600, the redshifts changed to blueshifts at least in the optical, and some lines that had no redshifts developed blueshifts also. The redshifts can be explained by electron scattering of line-emitted flux (e.g., B88; Witteborn et al. 1989). Line photons scattered into the line of sight by electrons that are moving away from the point of photon emission will exhibit a redshift. Therefore, in addition to the direct line emission flux, there could be an electron-scattered, polarized, redshifted line emission flux. B88's polarization data for day 350 (see above) strongly support this explanation, since they show that some line-emitted flux was polarized and that the polarized intensity profiles for the lines were somewhat redshifted from their line flux profiles. The polarization is almost certainly due to electron scattering, since the flux line profiles in B88's flux spectrum for day 350 are almost pure emission-line profiles and these should not give rise to line polarized flux (see the argument in § 5). As mentioned in § 5, significant scattering by electrons should disappear sometime of order day 300 (the beginning of the full nebular phase), and thus so should the redshifting effect. Therefore, the disappearance of the redshifts some hundreds of days after the explosion should have been expected. However, the subsequent blueshifts, which have been explained as due to the formation of dust in the ejecta (Lucy et al. 1989), show that a complicating effect is operating. Clearly,

TABLE 2

PARAMETERS OF THE SYNTHETIC-SPECTRUM CALCULATIONS

Figure	Day	n_{el}	v_{ph} (km s^{-1})	T (K)	r_{core}	R	τ_{core}(con)	X_{ph}	c/a
8	11–12	...	5700	6030	0.56	∞	10	0.2	1.07
9	12	...	5400	5970	0.57	∞	10	0.2	1.05
10–11	100	0	1460	5120	1.0	5	1	0.4	1.11

NOTE.—The quantity n_{el} is the index of the inverse power law describing the radial electron density distribution. For calculations for which n_{el} is not specified, the radial electron density distribution was assumed to scale with the JB homologous density distribution (see § 3.1). When the outer cutoff radius R is specified to be infinity, all that is meant is that the actual calculational R is sufficiently large that making R larger has negligible effect on the synthetic spectra.

one cannot be sure that significant electron scattering vanishes when the redshifts vanish. However, as discussed in § 5, the time independence of the polarization spectrum observed at the La Plata Observatory over the 6 month period around day 650 suggests that significant intrinsic polarization and thus significant electron scattering had vanished by that time.

6.2. *Synthetic-Spectrum Analysis*

Using the heuristic model, synthetic flux and polarization spectra have been calculated to fit a small sample of the ISP–corrected narrow-band polarimetric and spectropolarimetric data taken during the photospheric epoch of SN 1987A. Some of the more important parameters for the synthetic spectrum calculations are displayed in Table 2. The procedure adopted for fitting the observations is as follows. A synthetic flux spectrum was fitted to an observed flux spectrum by varying the photospheric optical depths; the optical depth values calculated by JB were used as starting values. The scale of the synthetic flux spectrum was determined by requiring that the integrals over some appropriately chosen wavelength range of the synthetic and observed flux spectra be equal. The goodness of the fit was judged by eye. Having fitted the flux spectrum, the c/a parameter was adjusted in order to fit the continuum polarization level. For the calculations for Figures 8 and 9, the JB homologous density distribution was used for both the line and electron opacity, and the core continuum optical depth was set to 10 in order to simulate a deep scattering atmosphere. For the calculations for Figures 10 and 11, the JB homologous density distribution was used for the line opacity, a constant density distribution was used for the electrons, and the core continuum optical depth was set to 1.

Shown in Figure 8 are narrow-band and broad-band polarimetry reported by Schwarz (1987b) for days 11–12 (1987 March 6–7 UT). In Schwarz's paper, the data are given a slightly different ISP correction than the one used here. The central wavelengths and FWHMs of Schwarz's narrow-band filters are given in Table 3. Each filter is labeled by a P Cygni line feature (e.g., Hα absorption) that at least in some epoch of the SN 1987A evolution is sampled by that filter. The uncertainty in Schwarz's narrow-band fractional Q and U parameters is taken to be 0.07%; this is the value given by Schwarz & Mundt (1987) as a typical uncertainty in the earliest data reported by Schwarz (1987b). The vertical error bars of the ISP–corrected narrow-band data points are derived using the 0.07% value and the usual first-order error propagation formulae. No uncertainty has been assigned to the La Plata ISP. The broad-band data are plotted in order to give some idea of the continuum polarization. The prescription adopted for plotting the broad-band data is as follows. The wavelength at the center of the FWHM region of a broad-band filter is defined in this paper as the central wavelength of that filter and is used as the wavelength coordinate for the broad-band data points for the filter. The horizontal error bars of the broad-band data points display the FWHM region. The broad-band filter characteristics (i.e., central wavelength and FWHM) were taken from Lamla (1982). Schwarz reports he used the Cousins *UBVRI* system filters. However, the Johnson filter characteristics were used here for the *UBV* bands, since the Cousins *UBV* filter characteristics were not readily available. The broad-band filter characteristics are shown in Table 3. The uncertainties in the broad-band data points are derived from the uncertainties given by Schwarz (1987a), with again no uncertainty assigned to the La Plata ISP. (Schwarz 1987a is the original report of

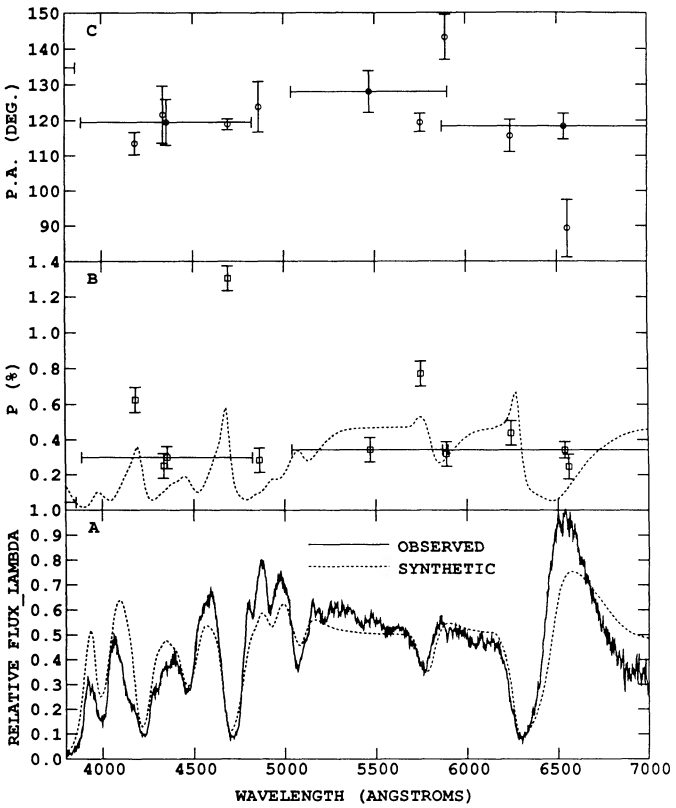

FIG. 8.—ISP–corrected narrow-band and broad-band polarimetry (3800–7000 Å) for days 11–12 (1987 March 6–7 UT) from Schwarz (1987b), the flux spectrum for day 11.76 (1987 March 6.08 UT) from Phillips et al. (1988), and fitted synthetic flux and polarization spectra.

TABLE 3

CHARACTERISTICS OF THE NARROW-BAND AND BROAD-BAND FILTERS

Filter	Central Wavelength (Å)	FWHM (Å)
Hα emission	6565	10
Hα absorption	6251	33
Hβ emission	4867	34
Hβ absorption	4697	10
Hγ emission	4340	28
Hγ absorption	4188	33
Na D emission	5897	56
Na D absorption	5757	20
U	3500	700
B	4350	950
V	5500	850
R	6550	1350
I	8100	1650

NOTE.—The characteristics of the narrow-band filters were obtained from Schwarz 1987b. The broad-band filter characteristics are taken from Lamla 1982. The *UBV* characteristics are for filters from the Johnson system. The *RI* characteristics are for filters from the Cousins system. The central wavelength of a broad-band filter is defined in this paper to be the wavelength at the center of the FWHM region of the broad-band filter.

the days 11–12 broad-band data. The data values in Schwarz 1987a are not quite the same as in Schwarz 1987b; the data probably had not been given final reduction in Schwarz 1987a.) The observed flux spectrum shown in Figure 8*a* was reported by Phillips et al. (1988).

The synthetic flux spectrum fit in Figure 8*a* is reasonably good. The observed Hα P Cygni line profile shows a net emission that cannot, of course, be reproduced using pure resonance scattering. The blueshift exhibited by the observed Hα emission maximum from the Hα line-center wavelength is also an effect not obtainable from pure resonance scattering. The synthetic polarization spectrum fit in Figure 8*b* is not impressive. The line features are qualitatively but not quantitatively consistent with the data. It is particularly noticeable that the synthetic Hβ, Hγ, and Na D line trough features are too weak. These trough features could easily be made stronger by increasing the c/a value, but then the rough fit to the observed continuum polarization would be lost and the Hα observations would be fitted more poorly. The synthetic continuum polarization shows a reduction in going from the *V* band to the *B* band. This reduction is due to the effect of the overlapping lines; the depolarizing effect of the emission regions of the line profiles dominates over the polarization increases associated with the line troughs. Why this overlapping line effect is not apparently operative in the formation of the observed polarization spectrum is not clear.

Two possibilities exist for achieving a consistent line and continuum fit: (1) using a realistic model would probably give higher trough polarization maxima relative to the continuum polarization level (see Figs. 5–6); (2) the electron density distribution can be made more extended (i.e., less steep) than the homologous density distribution used to describe the line opacity. An investigation of the first possibility is deferred to future research. The second possibility increases the line trough polarization maxima by having more electron flux scattered farther out in the limb where the depolarizing effect of the line CD velocity surfaces is weaker. Making the electron density distribution more extended will also increase the continuum polarization. Whether the line trough polarization increases relative to the continuum polarization probably has to be determined separately for each case considered (see the discussion of Figs. 10 and 11 below).

Figure 8*c* shows the position angles for the polarization data. Here and in Figures 9–11, the freedom to add and subtract multiples of 180° from the position angles was used in order to try to minimize oscillations in the position-angle data. Since the position angle of polarization for the heuristic model must be a constant and this constant can be assigned to any value arbitrarily, there was no point in plotting a heuristic model synthetic position-angle spectrum in Figure 8*c* or in subsequent position-angle figures. The position-angle behavior seen in Figure 8*c* is typical for the photospheric epoch: i.e., an identifiable continuum position angle consistent with the 100°–130° range and rather sharp non-90° shifts in position angle across some of the line profiles (see § 6.1, Figs. 9–11, and Jeffery 1991).

Shown in Figures 9–11 are flux spectra and spectropolarimetry reported by Cropper et al. (1988) for day 12 (1987 March 7 UT) and day 100 (1987 June 3 UT). Cropper et al. report spectropolarimetry for seven other days in the photospheric epoch of SN 1987A. All the Cropper et al. spectropolarimetry corrected with the La Plata ISP is shown in Jeffery (1991). The polarization data displayed in Figures 9–11 are binned in wavelength in order to keep the statistical uncertainty in the polarization of order 0.1% or less. The systematic uncertainty due to the uncertainty in the adopted ISP can, of course, make the error in the displayed data larger than 0.1%.

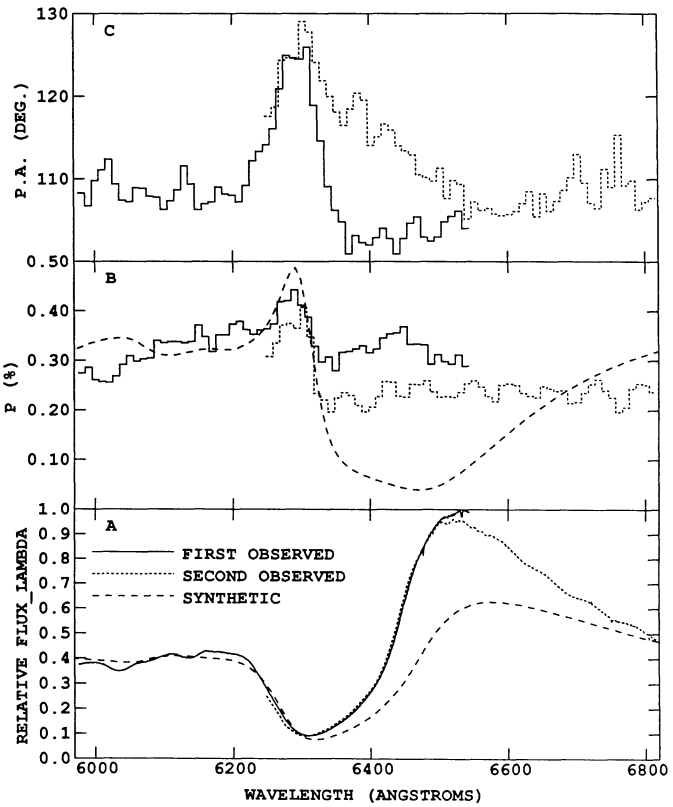

FIG. 9.—ISP–corrected spectropolarimetry and flux spectrum (5970–6820 Å) for day 12 (1987 March 7 UT) from Cropper et al. (1988) and fitted synthetic flux and polarization spectra. The polarization data are binned in 10 Å wavelength intervals. The statistical uncertainty in the observed polarizations is of order 0.1%.

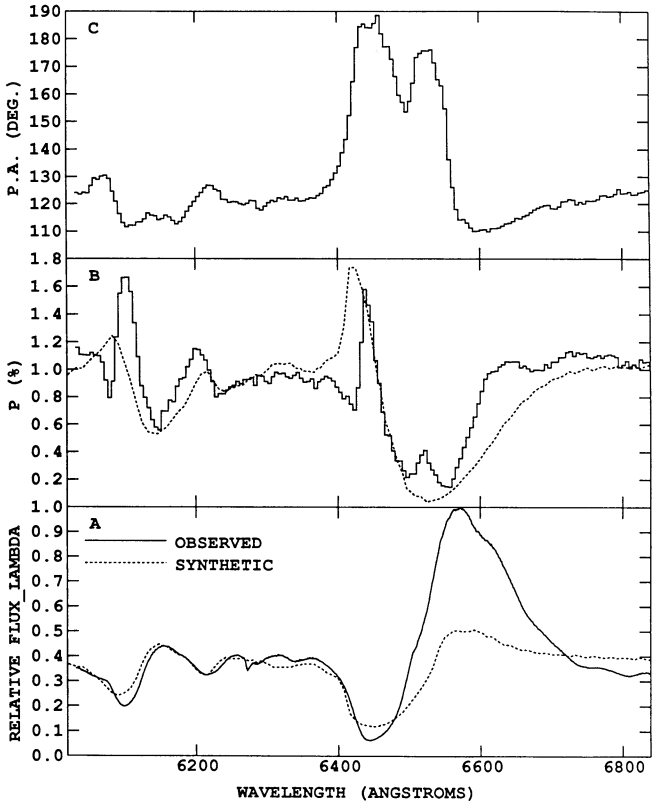

FIG. 10.—Same as Fig. 9, but for day 100 (1987 June 3 UT), with wavelength interval 6020–6840 Å and with polarization binning interval 5 Å.

The remarks made about the synthetic flux spectrum fit in Figure 8*a* also apply to the synthetic flux spectrum fit in Figure 9*a*. The synthetic polarization spectrum fit is reasonable for the continuum polarization and the polarization maximum. The polarization dip across the line flux emission that appears in the synthetic polarization spectrum, however, is not evident in the observed polarization spectrum; the reason for this discrepancy is not known.

The polarization data for day 100 displayed in Figures 10–11 show several interesting features. The continuum polarization is ~1%; only a few broad-band polarizations, notably the day 262 *JHKL* polarizations, are significantly higher than about 1%. The line trough polarization maximum of the Ca II triplet ($\lambda\lambda$8498, 8542, 8662) is ~4%. This is the highest polarization seen in the ISP–corrected polarization data by a factor of about 2. There is a very noticeable difference in the position-angle behavior of the Hα line and the Ca II triplet: the Hα trough position angle is strongly shifted from the continuum position angle; the position angle across most of the Ca II triplet profile appears to show a weaker shift in the opposite direction. The position-angle distinction between the Hα line and the Ca II triplet is evident in the uncorrected polarization data and was noted by Cropper et al. (1988). Besides the Hα line and the Ca II triplet polarization features, there are also line polarization features associated with the line profile identified as Ba II λ6142 and the line profile that probably results from a blend of Fe II lines with line-center wavelengths near 6250 Å (see, e.g., Höflich 1988, Fig. 3; JB, Fig. 34*a*).

The synthetic flux spectra calculated for Figures 10–11 are not in particularly good agreement with the observed Hα and Ca II triplet line profiles. Both these observed line profiles show net line emission which cannot be obtained from pure resonance scattering. In order to get the flux troughs of the strong lines (i.e., the Hα and Ca II triplet lines) as well fitted as they are, an outer cutoff radius had to be adopted that is well short of the known lower limit of the radius of the outermost SN 1987A ejecta. The need for an outer cutoff radius suggests that the excitation of strong lines falls off more steeply with radius than the JB homologous density distribution. The core continuum optical depth adopted for this calculation was only 1. A larger core continuum optical depth was not used simply for computational economy; such a larger depth would have increased the continuum polarization for a given c/a value. In order to obtain the trough polarization maxima for the stronger lines, the electron density distribution had to be made more extended than the JB homologous density distribution. Without this more extended electron density distribution, the CD velocity surfaces of the strong lines were sufficiently strong over a sufficiently broad region that they reduced polarization at the line profile troughs below the continuum polarization, even though they also reduced unpolarized photospheric flux. Making the core continuum optical depth larger would not have given trough polarization maxima; it would have increased the electron-polarized flux from the limb, but this flux would still be scattered from too near the photosphere to escape depolarization in the CD velocity surfaces of the strong lines. In order to obtain the trough polarization maxima, significant limb scattering by electrons had to be put farther out in the atmosphere. For the displayed synthetic polarization spectra, this was done by making the electron density constant throughout the atmosphere. These synthetic polarization

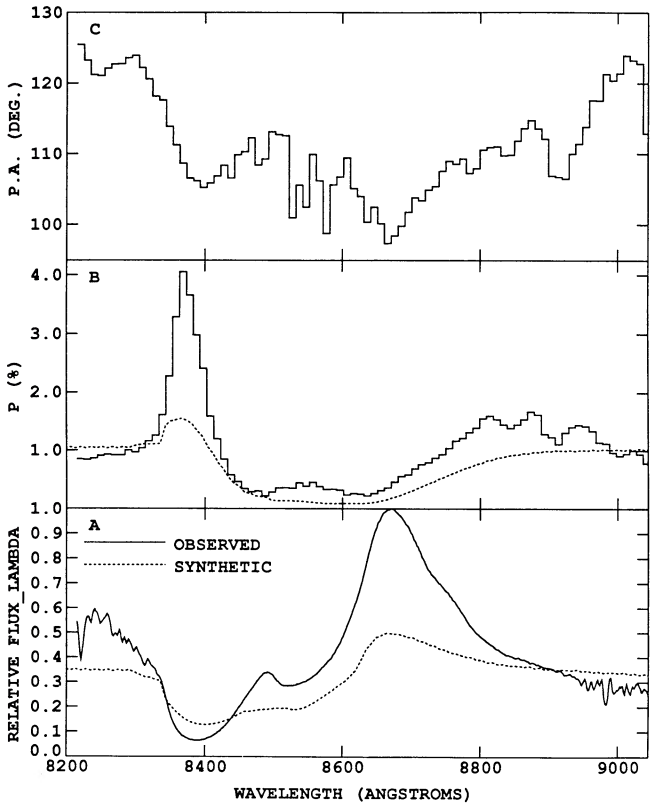

FIG. 11.—Same as Fig. 10, but with wavelength interval 8200–9045 Å and polarization binning interval 10 Å.

spectra show rough qualitative agreement with the observations. There are, however, considerable discrepancies, notably between the heights of the observed and synthetic Ca II triplet polarization maxima.

The discrepancies between the observed and synthetic polarization spectra are at least in part owing to the poorness of the synthetic flux spectrum fit. However, to fit the high Ca II triplet polarization maximum probably requires more than simply deepening the primary Ca II triplet trough. It seems likely that some special excitation asymmetry is required for the Ca II triplet. The already noted distinction between the position-angle behavior of the Hα and Ca II triplet profile polarizations also suggests excitation asymmetries. It seems unlikely that this distinction can be entirely due to the formation of these line profiles in different spatial regions with different density asymmetries. The wavelength range of the Hα trough position angle that plateaus at about 170° corresponds roughly to a line-of-sight velocity range of 0–7500 km s^{-1}. The wavelength range of the Ca II triplet profile position angle of about 110° corresponds roughly to a line-of-sight velocity range of about 0–6000 km s^{-1} at least. One can see that the CD velocity surfaces that give rise to the Hα and Ca II triplet polarization features are spread over much the same region of ejecta. It seems unlikely that hydrogen and calcium could have distinct compositional asymmetries. Therefore, the distinctions in the position angles are probably due to distinct excitation asymmetries. The day 100 wavelength range of the Na D lines' trough position angle that plateaus at about 150° (see Jeffery 1991, Fig. 14) corresponds roughly to a line-of-sight velocity range of 0–6500 km s^{-1}. Since the Na D trough position-angle shift is different from the position-angle shifts associated with the Hα line or the Ca II triplet, the Na D trough position angle behavior supports the idea of excitation asymmetries. The position angle shifts across line profiles on other days are probably also at least partially due to excitation asymmetries.

The present analysis cannot say anything definitive about the nature or the size of the SN 1987A asymmetry. The c/a values required to fit the continuum polarizations are 1.07, 1.05, and 1.11 (see Table 2). The 1.11 value is probably an overestimate because it was determined from a spectrum-fit calculation that did not use a deep scattering atmosphere. Since the heuristic model is not actually a very plausible model for the supernova, one would like to have a c/a value determined from a realistic model fit. From Figures 5 and 6, one can see that to fit a continuum polarization of 0.2% with realistic models with inverse power law indices of order 4 or higher would require $c/a \sim 0.8$ for an oblate model calculation; numerical experiments suggest that one would need $c/a \sim 1.2$ for a prolate model calculation. The continuum polarizations on days 11–12 were of order 0.3%. The photospheric density gradient of the ejecta at this epoch is possibly approximated by an inverse power law of index ~ 5 (see JB, Fig. 15). Thus, if the realistic model is valid for SN 1987A, a length-width difference of order 10% or more would be attributed to SN 1987A. Méndez et al. (1988) and Höflich et al. (1989), from analyses of the SN 1987A broad-band polarimetry using models similar to the realistic model, determined length-width difference ranges of 10%–20% and 5%–10%, respectively. These groups of authors used ISP corrections different from that used here and from each other. With these corrections the order of magnitude of the broad-band polarization is roughly the same as one obtains with the La Plata ISP correction, but the temporal evolution is different. The asymmetry estimates of Méndez et al. and Höflich et al. would probably not change greatly if they had used the ISP correction adopted here. Using still another different ISP correction and very simple models, Cropper et al. (1988) estimated length-width asymmetries in the range 5%–30%. All these asymmetry estimates are consistent with the estimate of 20% length-width difference made in § 6.1. An early analysis of the SN 1987A days 11–12 narrow-band polarimetry by Jeffery (1987) determined a length-width difference range of 20%–40%; this analysis has to be discounted, however, since electron polarizing scattering, which is now thought to be the dominant polarizing effect, was not included in the calculations.

The above discussion makes it plausible that if SN 1987A exhibits a simple length-width shape asymmetry, then this asymmetry needs to be of order 10% or more. However, in the discussion of day 100 spectropolarimetry, it was concluded that excitation asymmetry was probably needed to explain the line polarization features. There is another piece of strong evidence that excitation asymmetry is present in SN 1987A. In a period starting at about day 20 and lasting until some time after day 111, satellite emission features appeared superposed on the ordinary emission features of several lines, most notably on the Hα line emission feature. These satellite emission features have been collectively called the Bochum event after the university, Ruhr-Universität Bochum, of some of the discoverers (see Cristiani et al. 1987; Hanuschik & Dachs 1987). The Bochum event is well described and discussed by Phillips & Heathcote (1989). The Bochum emission features were located at wavelengths that were blueward and/or redward from the line-center wavelength. In the case of the Hα line, both blue and red Bochum emission features were clearly present and were symmetrically displaced from the Hα line-center wavelength. To explain the Bochum event, Lucy (1988) suggested that there could be an equatorial band in the supernova where there is an enhancement of the hard radiation from the radioactive ^{56}Co that powers the supernova after a few tens of days after the explosion. This radioactive band may be due to an equatorial abundance enhancement of the ^{56}Co. The radioactive band could give rise to the symmetric Bochum emission features and could give rise to an excitation asymmetry that would cause the observed polarization behavior. Of course, the band could not be purely axisymmetric, since the discussion above of position-angle behavior has ruled out pure axisymmetry. The hypotheses of a radioactive band asymmetry and of a simple shape asymmetry are not mutually exclusive.

Another striking piece of evidence that can support either the radioactive band or the shape asymmetry hypotheses is provided by the speckle imaging reported by Karovska et al. (1988, 1989b). Karovska et al.'s images of SN 1987A taken from day 95 to day 411 showed that the supernova was elongated along the direction 20° ± 5° measuring clockwise from north; the variation of the elongation direction with wavelength was less than 10°. This direction is, of course, shifted ~90° from the special polarization axis of about 115° discussed in § 6.1. The length-width difference of the speckle images is between 10% and 40% depending on the wavelength of observation. The southwest ends of the elongated images were somewhat brighter than the northeast ends. The speckle images grew in size at about 3000 km s^{-1} (Karovska et al. 1989a, Fig. 8). Both the radioactive band and an elongated atmosphere may be able to explain the elongated speckle images. In the heuristic and realistic models, the position angle of polarization aligns with the long axis of the model. There-

fore, the fact that the special polarization axis is aligned roughly perpendicular to the long axis of the speckle images opposes a simple heuristic or realistic model interpretation of the SN 1987A asymmetry. It is, however, probably not difficult to construct a simple axisymmetric model which would yield a polarization position angle 90° shifted from the model's elongation axis. The fact that there are two special SN 1987A axes that are separated by roughly 90° does suggest that SN 1987A has an axisymmetric component and therefore that axisymmetric models are partially viable. It remains to be seen whether simple axisymmetric radioactive band models can give explanations of both the special polarization axis and the elongated speckle images.

6.3. *Origin of the SN 1987A Asymmetry*

Although the origin of the SN 1987A asymmetry is not known, several possibilities can be considered. The first possibility is that the asymmetry is due to the clumping of ejecta material caused by turbulent mixing. The unexpectedly early appearance of X-rays and γ-rays from SN 1987A (see, e.g., Sutherland 1990 and references therein) has an explanation in such turbulent mixing of the helium core ejecta and the hydrogen envelope ejecta. This mixing transports radioactive ^{56}Co into the outer supernova ejecta, where X-rays and γ-rays from the ^{56}Co decay can escape more freely than from the deep ejecta (e.g., Itoh et al. 1987). The cause of the mixing is very probably Rayleigh-Taylor instability during the supernova explosion (e.g., Benz & Thielemann 1990). Calculations of the Rayleigh-Taylor mixing (Nomoto et al. 1991) gives clumps that have a size scale that may be too small if the clumps are produced in a roughly spherically symmetric array to account for the polarization, Bochum event, and speckle image observations. Such a spherically symmetric array of small clumps would give the supernova an overall spherical symmetry.

Rotation of the SN 1987A progenitor is a plausible source for large-scale axisymmetric asymmetry of the supernova ejecta. However, what region of the rotating progenitor could be the origin of the asymmetry and what the nature of that asymmetry would be are still open subjects of study. Chevalier & Soker (1989) find that rotation of the envelope of a SN 1987A progenitor can produce length-width differences in the 10%–30% range; the density contours in their results have prolate asymmetry in the outer ejecta and oblate asymmetry in the inner ejecta. However, to produce so large an asymmetry, they required so much angular momentum that a binary companion star to the progenitor would need to be invoked to supply angular momentum through tidal interaction. Yamada & Sato (1990) invoked a rotating O-Ne-Mg core as the source of SN 1987A asymmetry and found that asymmetries of order 20%–50% could be produced in the ejecta. They found larger asymmetry when the initial iron core explosion was made asymmetric and also verified that the asymmetry did not damp out as the explosion propagated through the hydrogen envelope. Yamada & Sato's asymmetries will probably be of a prolate type, but they did not publish final density contour plots for the ejecta. Iron core-collapse calculations that include rotation have found that significant and complicated asymmetries can arise in the collapse event (e.g., Müller & Hillebrandt 1981; Symbalisty 1984, 1985). Provided that asymmetric core collapses occur, Yamada & Sato's calculations suggest that the asymmetry should propagate to the outer ejecta. Chevalier & Soker, however, find that asymmetries arising from core explosions tend to be damped out in propagating through model envelopes devised to represent red supergiants, the probable progenitors of most SN II's. This damping-out effect probably becomes smaller as the progenitor star envelope becomes more compact. The fact that the SN 1987A progenitor was a blue supergiant and consequently had a relatively compact envelope would thus probably aid the propagation of core-generated asymmetries. Chevalier & Soker also find that envelope compactness enhances the asymmetry effects of envelope rotation.

One can imagine that a radioactive band asymmetry described above could be produced by a globally asymmetric Rayleigh-Taylor mixing. The seed for this globally asymmetric Rayleigh-Taylor mixing might be envelope or core rotational asymmetries. Perhaps the combination of the mixing and rotation effects can lead to sufficiently large asymmetries without the necessity of invoking implausible progenitor or explosion conditions.

Another possible origin for asymmetry is mixing that occurs after the explosion (Woosley 1988). The energy released slowly by the radioactive elements will have dynamic effects on a time scale of the order of 100 days. The layers where the radioactive elements are deposited are expected to be Rayleigh-Taylor unstable, at least in calculations that do not account for asymmetries or the explosion epoch Rayleigh-Taylor mixing. Whether this postexplosion mixing actually occurs or can create large enough asymmetries to account for some of the observations is not known. If there were no explosion-epoch mixing, then the radioactive elements would probably be located in deep ejecta moving at ~ 1000 km s^{-1} (Woosley 1988). Acting by itself, the slow postexplosion mixing of this deep ejecta probably cannot explain the days 11–12 polarimetric data, since the photosphere in the days 11–12 epoch was in matter moving at ~ 5000 km s^{-1} (see Table 2).

Asymmetric post–explosion-epoch mixing has been invoked to explain the nebular phase redshifts and blueshifts exhibited by some of the prominent emission-line features (Spyromilio, Meikle, & Allen 1990). However, the explanation for these shifts that uses electron scattering and dust formation (see § 6.1) seems to be favored.

7. CONCLUSIONS AND DISCUSSION

The analysis of this paper can be summarized with several conclusions. (1) The SN 1987A continuum polarization and line polarization features are mostly due to the polarizing effect of electron scattering. The intrinsic line polarizing effect may be operative, but it can only be of secondary importance and probably can only contribute to the polarization of the net flux in the photospheric phase. (2) The asymmetry of SN 1987A cannot be purely axisymmetric. Two special axes do, however, exist that are separated by roughly 90°. This fact suggests that SN 1987A may have an axisymmetric component. (3) In agreement with other researchers, an interpretation of the SN 1987A polarimetric data in terms of simple shape asymmetry requires that SN 1987A have a length-width difference of order 10% or more. This order of asymmetry is consistent with the speckle image observations. (4) There is evidence from the line polarization position-angle features and the Bochum event for an excitation asymmetry. Such an excitation asymmetry has a possible explanation in a radioactive band. A radioactive band asymmetry does not exclude the possibility that a simple shape asymmetry exists also.

In future work, a complete analysis of all the SN 1987A polarimetry should be carried out using more plausible models

than those used for this paper. These new models could be made to incorporate the asymmetries suggested by the asymmetric hydrodynamic supernova calculations and radioactive band asymmetries. They could also be made to include features of the SN 1987A atmosphere predicted by the NLTE calculations (e.g., Höflich 1988; Eastman & Kirshner 1989). An analysis using such models may lead to an identification of a most probable sort of asymmetry and to an estimate of this asymmetry's size. Further constraints on the SN 1987A asymmetry that would help in analyzing the polarization data may be provided by the *HST* imaging of the SN 1987A ejecta that the SINS (Supernova INtensive Study) collaboration hopes to perform (Kirshner et al. 1988).

Besides SN 1987A, there are only two other supernovae for which spectropolarimetric data exist: SN 1983G, a SN Ia (McCall *et al.* 1984), and SN 1983N, a SN Ib (McCall 1985). The published polarization spectrum for SN 1983G shows apparent polarization maxima associated with some of the P Cygni line troughs. The observers, however, thought that the statistical uncertainty in the data was too large to attribute any significance to the apparent line polarization features. No published polarization spectrum has appeared for SN 1983N. McCall reports, however, that there was a continuum polarization of 1.4% and that the polarization dipped to 0.8% at about 4600 Å, where the emission peak of a blend of Fe II lines was located. The size of this line polarization feature is comparable to the size of line polarization features in the SN 1987A data. This suggests that SN 1983N had an asymmetry comparable to the SN 1987A asymmetry. If the hypothesis is correct that SN Ib's are the results of core collapses in massive stars that have lost their hydrogen envelopes and thus are compact (e.g., Wheeler & Levreault 1985), then there are two asymmetry detections out of two attempts to detect asymmetry in the supernovae resulting from core collapses of compact progenitors. Consequently, the conjecture can be made that all compact-progenitor core-collapse explosions have significant asymmetry. The asymmetry effect may also be present in the core collapses of progenitors with extended envelopes. However, as discussed in § 6.3, asymmetry probably tends to be damped out in such cases. If one supposes that the asymmetry effect is present in all core-collapse explosions, then the question immediately arises whether the asymmetry effect is merely incidental or is fundamentally important to the nature of core-collapse explosions.

Given the great uncertainties about supernova asymmetry, further analyses of the existing supernova polarimetry are merited, and the acquisition of new polarimetry, especially spectropolarimetry, of all sufficiently bright supernovae is recommended.

I thank Hugo E. Schwarz of the European Southern Observatory, Jeremy A. Bailey and Russell D. Cannon of the Anglo-Australian Observatory, and Mariano Méndez of the La Plata Observatory for providing me with data. I also thank David Branch for encouraging me to write this paper, Peter Höflich for a helpful discussion in Santa Cruz, and the referee for his suggestions. The research for this paper was supported by the University of Oklahoma and by NSF grant AST 8620310 (to David Branch).

APPENDIX

SCATTERING IN THE SOBOLEV-P METHOD PICTURE

In order to help understand scattering and scattering's polarizing effect in the physical picture of the Sobolev-P method, some simple analytical expressions can be presented.

In the Sobolev method, the directional escape probability and the escape probability (short for angle-averaged escape probability) for a resonance region are given by

$$\beta_d = \frac{1 - e^{-\tau}}{\tau} \quad \text{and} \quad \beta = \oint \frac{d\Omega}{4\pi} \beta_d \,, \tag{A1}$$

respectively, where τ is the direction-dependent Sobolev optical depth of the resonance region. The quantity β_d can still be interpreted as the directional escape probability in the Sobolev-P method, since it is a conditional probability: i.e., given that a line emission occurs in the resonance region in a specified direction, β_d evaluated for that direction is the probability that the photon escapes the resonance region without interacting with the line again. It is with this conditional probability interpretation that the appearance of β_d in Sobolev-P expressions in SPM II and SPM III is to be understood. (The β quantity also appears in Sobolev-P expressions in these papers, but only as a symbol for β_d when β_d is direction-independent.) In general, β cannot be considered a good definition of the Sobolev-P escape probability because it does not include a factor to account for the angle dependence of resonance scattering emission. A definition of a mean escape probability appropriate for the Sobolev-P method is

$$B = \oint d\Omega \, S\beta_d \Big/ \oint d\Omega \, S \,, \tag{A2}$$

where S is the source function. In the Sobolev-P method, the source function is, of course, not in general isotropic as it is in the Sobolev method. The mean escape probability does not apply to any single scattering event. For each scattering event, the escape probability will in general depend on the propagation direction and polarization of the incident photon, since the angular variation of the scattering phase function depends on these incident-photon properties. The B quantity is only an average over all scatterings of all photons. If S is isotropic, B reduces to β. In this case, B is still in general only a mean escape probability, since an isotropic S does not necessarily imply isotropic scattering. For example, a resonance region with a very large optical depth will have a source function that approaches isotropy even though there may be an anisotropic scattering probability for individual scattering events (see SPM III). If β_d is direction-independent, then B reduces to β_d and does apply to individual scattering events. In this case, the

angular integration for the escape probability is only over the scattering phase function, which is normalized to 1. Homologous expansion is an example of a case where β_d is direction-independent.

An expression for the mean number of scatterings that a photon undergoes in a resonance region will be obtained for a simple special case. Consider a monochromatic specific intensity beam propagating in some direction. At some point this beam encounters the resonance region for its wavelength. In this resonance region, only pure resonance scattering occurs. The β_d quantity is assumed to be direction-independent. The probability that a photon from the beam is scattered n times in the resonance region is

$$P_n = \begin{cases} e^{-\tau} & \text{for } n = 0 , \\ (1 - e^{-\tau})\beta_d(1 - \beta_d)^{n-1} & \text{for } n > 0 , \end{cases} \tag{A3}$$

where $e^{-\tau}$ is the probability that a photon passes through the resonance region without scattering. The mean number of scatterings and the standard deviation of the scattering probability distribution are given by

$$\langle n \rangle = \tau \tag{A4}$$

and

$$\sigma = \left\{ \tau + \tau^2 \left[\frac{2(1 - \beta_d)}{1 - e^{-\tau}} - 1 \right] \right\}^{1/2} , \tag{A5}$$

respectively. The limiting cases for σ are given by

$$\sigma \approx \begin{cases} \sqrt{\tau} & \text{for } \tau \ll 1 ; \\ \tau & \text{for } \tau \gg 1 . \end{cases} \tag{A6}$$

From equation (A3), one can see that the scattering probability distribution is rather slowly varying with n for large τ. If the further assumption is made that the incident beam is unpolarized, then the system is axially symmetric about the incident beam's propagation direction. Let the Stokes l- and r-axes for each beam emergent from the resonance region be taken to be in and perpendicular to, respectively, the plane defined by the emergent and incident beams. With this specification, the axial symmetry implies that the emergent beam has a zero Stokes U parameter and that, using equations (1) and (2), the emergent beam's polarization is given by

$$P = |I_l - I_r|/I . \tag{A7}$$

(Note that the convention of measuring polarization in percent has been dropped for the discussion in this appendix.) The mean polarization that a photon acquires in passing through the resonance region is given by

$$P = (1 - e^{-\tau}) \oint d\Omega \left(S \Big/ \oint d\Omega' S \right) |(S_l - S_r)/S| , \tag{A8}$$

where $1 - e^{-\tau}$ is, of course, the probability that a photon is scattered in the resonance region, and S_l and S_r are the l and r components, respectively, of the source Stokes vector for the resonance region. The first factor in the integrand of equation (A8) is the probability distribution for emission from the resonance region, and the second is the polarization of the emitted radiation. Using axial symmetry and equations (9), (17), (23), (25), (35), and (A1) of SPM III, one finds that the mean polarization is given by

$$P(E_1, \tau) = \frac{(1 - e^{-\tau})^2}{\tau} \frac{\frac{1}{2}E_1}{1 - (\frac{7}{10})E_1(1 - \beta_d)} . \tag{A9}$$

Equation (A9) will be called the polarization function.

The behavior of the polarization function is of interest in understanding the polarizing power of a resonance region. For $\tau = 0$, the polarization function is zero. As τ increases from zero, there is at first a linear increase of polarization with τ; then the rate of increase slows, and a polarization maximum is reached at some τ_{max}. As τ increases from τ_{max}, the polarization function declines and asymptotically approaches a $1/\tau$ behavior. The behavior of the polarization function is easily interpreted. When τ is small, there is little scattering and little polarization. On the other hand, when τ is very large, photons scatter many times in the resonance region. The multiple scattering tends to randomize the directions and polarizations of the photons. Consequently, the emergent radiation field tends to be isotropic and unpolarized. One would expect that τ_{max} would be of order unity, so that photons scatter on average only a few times. Because of the exponentials in the polarization function, no analytic expression for τ_{max} can be given. However, the factor $(1 - e^{-\tau})^2/\tau$, which dominates the behavior of the polarization function, has a maximum at $\tau = 1.26$. For E_1 equal to 1 and 0.4, the polarization function has maxima at 1.92 and 1.42, respectively. Figure 12 displays the polarization function for E_1 equal to 1 and 0.4, and also displays quantities related to the polarization function. Although the polarization function is the mean polarization a photon acquires only in a special case, one expects in general that the polarizing power of a resonance region will have the same sort of dependence on τ as does the polarization function. In general, however, the absolute size of the polarization of the emergent radiation field will also strongly depend on the isotropy of the incident radiation field. The more isotropic the incident radiation field is, the more isotropic and unpolarized the emergent radiation field will be.

In the DCO approximation (see § 2), converged flux and polarization solutions are obtained by decreasing the Sobolev optical depths of pseudolines. For this convergence procedure, it is convenient that the polarizing power of a resonance region has no rapidly varying dependence on τ. The absence of a rapidly varying τ dependence means that one does not have to worry about dramatic changes in polarization behavior when a solution is approaching convergence.

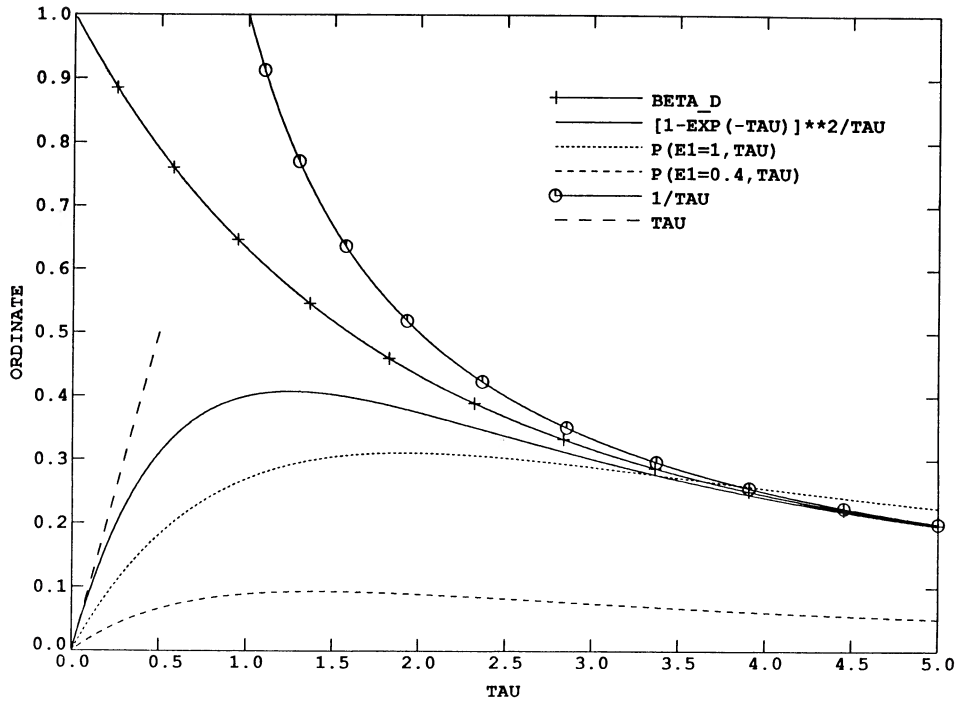

FIG. 12.—Polarization function $P(E_1, \tau)$ for E_1 equal to 1 and 0.4. Quantities related to the polarization function are also displayed.

REFERENCES

Axelrod, T. S. 1988, in Atmospheric Diagnostics of Stellar Evolution: Chemical Peculiarity, Mass Loss, and Explosion, ed. K. Nomoto (Berlin: Springer-Verlag), 375
Bailey, J. A. 1988, Proc. Astr. Soc. Australia, 7 (No. 4), 405 (B88)
Bailey, J. A., Ogura, K., & Sato, S. 1987, IAU Circ., No. 4351
Barrett, P. 1988, MNRAS, 234, 937
Benvenuto, O. G., Clocchiatti, A., Feinstein, C., Garcia, B., Luna, H., Méndez, M., & Morrell, N. 1987, IAU Circ., No. 4358
Benz, W., & Thielemann, F.-K. 1990, ApJ, 348, L17
Bionta, R. M., et al. 1987, Phys. Rev. Letters, 58, 1494
Branch, D., Doggett, J. B., Nomoto, K., & Thielemann, F.-K. 1985, ApJ, 294, 619
Branch, D., Pauldrach, A. W. A., Puls, J., Jeffery, D. J., & Kudritzki, R. P. 1991, in ESO Workshop on SN 1987A and other Supernovae (Garching: ESO), in press
Cassinelli, J. P., & Hummer, D. G. 1971, MNRAS, 154, 9
Catchpole, R. M., et al. 1987, MNRAS, 229, 15P
Catchpole, R. M., et al. 1988, MNRAS, 231, 75P
Chandrasekhar, S. 1960, Radiative Transfer (New York: Dover)
Chevalier, R. A., & Soker, N. 1989, ApJ, 341, 867
Clayton, G. C., Martin, P. G., & Thompson, I. 1983, ApJ, 265, 194 (CMT)
Clocchiatta, A., & Marraco, H. G. 1988, A&A, 197, L1
Code, A. D., Davis, J., Bless, R. C., & Hanbury Brown, R. 1976, ApJ, 203, 417
Cristiani, S., Gouiffes, C., Hanuschik, R. W., & Magain, P., 1987, IAU Circ., No. 4350
Cropper, M., Bailey, J. A., McCowage, J., Cannon, R. D., Couch, W. J., Walsh, J. R., Straede, J. O., & Freeman F. 1988, MNRAS, 231, 695
Cropper, M., Bailey, J. A., Peacock, T. I., & Wickramasinghe, D. T. 1987, IAU Circ., No. 4319
Daniel, J.-Y. 1978, A&A, 67, 345
Eastman, R. G., & Kirshner, R. P. 1989, ApJ, 347, 771
Feldt, A. N. 1980, Ph.D. thesis, Univ. Oklahoma
Hamann, W.-R. 1981, A&A, 93, 353
Hamilton, D. R. 1947, ApJ, 106, 457
Hanuschik, R. W., & Dachs, J. 1987, A&A, 182, L29
Hirata, K., et al. 1987, Phys. Rev. Letters, 58, 1490
Höflich, P. 1988, Proc. Astr. Soc. Australia, 7 (No. 4), 434
Höflich, P., Sharp, C. M., & Zorec, J. 1989, preprint
Itoh, M., Kumagai, S., Shigeyama, T., Nomoto, K., & Nishimura, J. 1987, Nature, 330, 233
Jeffery, D. J. 1987, Nature, 329, 419
———. 1988, Ph.D. thesis, McMaster Univ. (SPM I)
———. 1989, ApJS, 71, 951 (SPM II)
———. 1990, ApJ, 352, 267 (SPM III)
———. 1991, ApJS, in press
Jeffery, D. J., & Branch, D. 1990, in Jerusalem Winter School for Theoretical Physics, Vol. 6, Supernovae, ed. J. C. Wheeler, T. Piran, & S. Weinberg (Singapore: World Scientific), 149 (JB)
Karovska, M., Koechlin, L., Nisenson, P., Papaliolios, C., & Standley, C. 1988, IAU Circ., No. 4604
———. 1989a, ApJ, 340, 435
———. 1989b, in Highlights Astr., Vol. 8, ed. D. McNally (Dordrecht: Kluwer), 193
Karp, A. H., Lasher, G., Chan, K. L., & Salpeter, E. E. 1977, ApJ, 214, 161
Kirshner, R. P., Blades, J. C., Branch, D., Chevalier, R. A., Fransson, C., Wagoner, R. V., & Wheeler, J. C. 1988, *HST* Proposal SINS: The Supernovae INtensive Study
Lamla, E. 1982, in Landolt-Börnstein, New Ser., Group VI, Vol. 2b, Stars and Star Clusters, ed. K. Schaifers & H. H. Voigt (Berlin: Springer-Verlag), 35
Lucy, L. B. 1988, in Supernova 1987A in the Large Magellanic Cloud, ed. M. Kafatos & A. G. Michalitsianos (Cambridge: Cambridge Univ. Press), 323
Lucy, L. B., Danziger, I. J., Gouiffes, C., & Bouchet, P. 1989, in IAU Colloquium 120, Structure and Dynamics of the Interstellar Medium, ed. G. Tenorio-Tagle, M. Moles, & J. Melnick (Berlin: Springer-Verlag), 164
Magalhaes, A. M., & Velloso, E. W. 1987, IAU Circ., No. 4361
Martin, P. G. 1974, ApJ, 187, 461
McCall, M. L. 1984, MNRAS, 210, 829
———. 1985, in Supernovae as Distance Indicators, ed. N. Bartel (Berlin: Springer-Verlag), 48
McCall, M. L., Reid, N., Bessell, M. S., & Wickramasinghe, D. T. 1984, MNRAS, 210, 839
Méndez, M. 1990, private communication
Méndez, M., Clocchiatti, A., Benvenuto, O. G., Feinstein, C., & Marraco, H. G. 1988, ApJ, 334, 295
Mihalas, D. 1978, Stellar Atmospheres (San Francisco: Freeman)
Müller, E., & Hillebrandt, W. 1981, A&A, 103, 358
Nomoto, K., Shigeyama, T., Kumagai, S., & Yamaoka, H. 1991, in Supernovae: The Tenth Santa Cruz Summer Workshop in Astronomy and Astrophysics, ed. S. E. Woosley (New York: Springer-Verlag), 176
Olson, G. L. 1982, ApJ, 255, 267
Phillips, M. M., Hamuy, M., Heathcote, S. R., & Suntzeff, N. B. 1990, AJ, 99, 1133
Phillips, M. M., & Heathcote, S. R. 1989, PASP, 101, 137
Phillips, M. M., Heathcote, S. R., Hamuy, M., & Navarrete, M. 1988, AJ, 95, 1087
Rao, N. K., Raveendran, A. V., Joshi, U. C., & Vadher, N. M. 1987, IAU Circ., No. 4339
Rybicki, G. B., & Hummer, D. G. 1978, ApJ, 219, 654
Schmidt, Th. 1976, A&AS, 24, 357

Schwarz, H. E. 1987a, IAU Circ., No. 4339
———. 1987b, in ESO Workshop on the SN 1987A, ed. I. J. Danziger (Garching: ESO), 167
———. 1987c, private communication
Schwarz, H. E., & Mundt, R. 1987, A&A, 177, L4
Serkowski, K. 1973, in IAU Symposium 52, Interstellar Dust and Related Topics, ed. J. M. Greenberg & H. C. van de Hulst (Dordrecht: Reidel), 145
Shapiro, P. R., & Sutherland, P. G. 1982, ApJ, 263, 902
Sobolev, V. V. 1947, Moving Envelopes of Stars (Leningrad: Leningrad State Univ.) (English transl. by S. Gaposchkin [Cambridge: Harvard Univ. Press, 1960])
Spyromilio, J., Meikle, W. P. S., & Allen, D. A. 1990, MNRAS, 242, 669
Sutherland, P. G. 1990, in Supernovae, ed. A. G. Petschek (New York: Springer-Verlag), 111
Symbalisty, E. M. D. 1984, ApJ, 285, 729
Symbalisty, E. M. D. 1985, in Numerical Astrophysics, ed. J. M. Centrella, J. M. LeBlanc, & R. L. Bowers (Boston: Jones & Bartlett), 453
Wagoner, R. V. 1981, ApJ, 250, L65
Walker, A. R., & Suntzeff, N. B. 1990, PASP, 102, 131
Wampler, E. J., & Richichi, A. 1989, A&A, 217, 31
Wheeler, J. C. 1990, in Jerusalem Winter School for Theoretical Physics, Vol. 6, Supernovae, ed. J. C. Wheeler, T. Piran, & S. Weinberg (Singapore: World Scientific), 1
Wheeler, J. C., & Levreault, R. 1985, ApJ, 294, L17
White, G. L., & Malin, D. F. 1987, Nature, 327, 36
Wilking, B. A., Lebofsky, M. J., & Rieke, G. H. 1982, A.J., 87, 695
Witteborn, F. C., Bregman, J. D., Wooden, D. H., Pinto, P. A., Rank, D. M., Woosley, S. E., & Cohen, M. 1989, ApJ, 338, L9
Woosley, S. E. 1988, ApJ, 330, 218
Yamada, S., & Sato, K. 1990, ApJ, 358, L9